POST-SHOCK RELAXATION OF AIR SPECIES USING *AB-INITIO* DATA

A Thesis

by

ALEXANDER FANGMAN

Submitted to the Graduate and Professional School of
Texas A&M University
in partial fulfillment of the requirements for the degree of

MASTER OF SCIENCE

Chair of Committee,	Daniil Andrienko
Co-Chair of Committee,	Elaine Oran
Committee Members,	Freddie Witherden
Head of Department,	Ivett Leyva

December 2021

Major Subject: Aerospace Engineering

ABSTRACT

The intent of this work is to advance the current understanding of high-temperature chemical kinetics of air species under post-shock conditions. Quantum mechanical-based deterministic models, based solely on *ab-initio*-derived data, are used to assess coupled vibrational excitation and chemical reactions of air species at temperatures characteristic of hypersonic flight and reentry. The first post-shock simulations of *ab-initio* accuracy that resolve both atom-diatom and diatom-diatom interactions are presented. Comparisons of the constructed vibrational-specific state-to-state models are made to a rovibrational-based model to highlight the importance of atomic radicals in the collisional dynamics of high-temperature post-shock environments.

Recent shock-tube experiments, including those of Sharma and Gillespie (1991), Ibraguimova et al. (2013), and Streicher et al. (2021), are numerically simulated for purposes of model validation and to discuss drawbacks of current experimental data post-processing procedures and diagnostic techniques. Results from modeling Sharma and Gillespie's experiment indicate that the inclusion of energy transfer to electronically excited and ionic species is potentially required when attempting to deduce $N_2\,(X)$ vibrational temperatures through radiative signatures in pure nitrogen shock flows. Through comparisons with Streicher et al.'s data, it is shown that neglecting relaxation in the post-incident shock region may lead to non-negligible errors in determining initial post-reflected shock translational and vibrational temperatures and that the unsteady nature of the reflected shock front may need to be considered to accurately determine such quantities, particularly in cases where the test gas is not diluted with an inert species.

DEDICATION

To my family.

ACKNOWLEDGMENTS

There are many friends, colleagues, and mentors that have supported and encouraged me along the way. I would like to thank Dr. Daniil Andrienko for his guidance, patience, and understanding. I would like to thank the other members of my advisory committee, Dr. Elaine Oran and Dr. Freddie Witherden, for their support. And I would also like to thank Varishth Baluckram for mentoring me during my first year at Texas A&M and for inviting me to play giant UNO at Duddley's.

CONTRIBUTORS AND FUNDING SOURCES

Contributors

This work was supported by a thesis committee consisting of Dr. Daniil Andrienko and Dr. Elaine Oran of the Department of Aerospace Engineering and Dr. Freddie Witherden of the Department of Ocean Engineering.

Several comparisons to experimental and computational data from outside groups are made. Contributions from outside sources are clearly noted and cited within the text. The QCT calculations and post-processing of cross-sections were done by Dr. Daniil Andrienko and Varishth Baluckram. The numerical simulations of Ibraguimova et al.'s shock-tube experiment were done by Varishth Baluckram. All other work conducted for the thesis was completed by the student independently.

Funding Sources

Graduate study was supported by Graduate Research Assistantships from Texas A&M University.

NOMENCLATURE

a	Acceleration
C^{DV}	Vibration-dissociation coupling coefficient
D_e	Classical dissociation energy
D_v	Dissociation rate coefficient from vibrational state v
e_{vib}	Average vibrational energy
h	Internal enthalpy
h_f°	Standard enthalpy of formation
j	Rotational quantum number
$K_{v\rightarrow v'}$	Vibrational-translational rate coefficient from vibrational state v to vibrational state v'
k_b	Boltzmann constant
n_v	Number density of vibrational state v
p	Pressure
R_v	Recombination rate coefficient to vibrational state v
T	Translational temperature
T_v	Vibrational temperature
t	Time
u	Velocity
v	Vibrational quantum number
x	Distance
$\epsilon_{v,j}$	Energy of rovibrational state described by vibrational quantum number v and rotational quantum number j
ρ	Mass density

τ_{vib}	Vibrational relaxation time
$\dot{\omega}$	Species production term
χ	Mole fraction

ABBREVIATIONS

FF	'Frozen Frozen': Reflected shock numerical model which does not consider relaxation behind the incident or reflected shock-waves to determine initial post-reflected shock conditions at the observation location
ME	Master Equation
MT	Multi-Temperature (model)
NN	'Nonequilibrium Nonequilibrium': Reflected shock numerical model which considers relaxation behind both the incident and reflected shock-waves to determine initial post-reflected shock conditions at the observation location
PES	Potential Energy Surface
QCT	Quasi-Classical Trajectory (method)
TPS	Thermal Protection System
VT	Vibrational-Translational (energy transfer)
VV	Vibrational-Vibrational (energy transfer)

TABLE OF CONTENTS

Page

LIST OF FIGURES

FIGURE Page

LIST OF TABLES

TABLE Page

1. INTRODUCTION

1.1 Problem statement

As space and other national defense entities move toward more ambitious hypersonic vehicle and space programs [12], accurate numerical models capable of capturing the complex thermo-physical environments experienced by these hyper-velocity bodies have become increasingly crucial for mission success. From terrestrial-focused expeditions, to those aimed at studying our solar system on a grander scale [13, 14, 15], a number of challenges unavoidably arise during the numerical modeling and design stages of such hypersonic concepts. These challenges include determining optimal control strategies [16], engineering new methods of propulsion [17, 18], and adequately sizing thermal protection systems (TPSs) [19]. The present work seeks to aid in the latter through the development of high-fidelity aerothermochemistry models capable of accurately resolving high-temperature post-shock environments.

1.2 Background and motivation

Equilibrium of a gas state occurs when there is no net change in the properties of the system over time. In general, any perturbation of a molecular system from a state of thermal and chemical equilibrium requires a finite number of particle collisions to redistribute energy and reestablish a state of equilibrium. One such perturbation that dominates the flow field physics in supersonic and hypersonic flows is that of a shock wave. Behind a shock front, sharp gradients in thermodynamic properties arise as kinetic energy is transferred to the internal energy modes of molecules and atoms (i.e. the translational, rotational, vibrational, and electronic energy modes). Characterizing the time scales with which these internal energy modes equilibrate becomes increasingly important when they are of the same order as the fluid time scale, as chemical reaction rates, and thus flow compositions, are heavily dependent on the level of molecular excitation.

Heating loads are particularly sensitive to flow composition and material surface properties [20, 21, 22, 23]; therefore, accurately describing the post-shock and near-surface conditions around

a hypersonic vehicle or reentry capsule is pertinent for designing a TPS with minimal uncertainty. Because conditions in hypersonic ground testing facilities are limited [24] and flight testing is extremely costly, numerical models and simulations provide a powerful tool for developing next-generation hypersonic concepts.

To date, most numerical modeling campaigns undertaken during the design stage of a hypersonic vehicle or reentry capsule employ simplified models, such as Park's multi-temperature (MT) model [25]. Park's MT model is a phenomenological-based model derived from experimental data, which is often extrapolated outside of its intended range of applicability. This often leads to failures in accurately describing conditions in highly nonequilibrium environments [26]. Additionally, modeling new thermo-chemical states often requires a 're-tweaking' of the model parameters to better match experimental data.

The assumption inherent in all MT models is that the internal modes may be described by internal temperatures. As a result of this assumption, the influence of non-Boltzmann energy distributions is not readily captured. It has been shown previously that non-Boltzmann energy distributions can have a drastic impact on macroscopic quantities of interest under post-shock conditions. This includes dissociation rates in the fluid region around the hypersonic body [27] and recombination rates at the near-surface region [28, 29, 30]; both of which have a large impact on the predicted total surface heat flux.

To avoid the downfalls associated with legacy two-temperature models, deterministic models based on quantum mechanical principles have moved to the forefront of hypersonic fluid modeling research [2, 27, 31]. The proposed work seeks to further this field by developing vibrational-specific state-resolved relaxation models of air species, i.e. models which track the conservation of each quantum vibrational state of each molecular species, rather than employing a single conservation law for each particle species, thus providing a means for capturing the influence of non-Boltzmann physics.

Although vibrationally-resolved models have been reported before, e.g. [32], the proposed work will develop the first such models that are built using kinetic data of *ab-initio* accuracy and

resolve both molecule-molecule and molecule-atom collisions. Previous vibrationally-resolved models relied on (less than ideal) analytic models to determine rate coefficients of internal energy transfer for 4-body collisions, such as the Forced Harmonic Oscillator (FHO) model [33]. The development of the present *ab-initio*-based models eliminates the uncertainties imposed by these analytic models, thus providing a powerful means for analyzing the true physics of air species in the high-temperature environments characteristic of hypersonic flight.

1.3 Research objectives

This work has the following objectives:

- Construct vibrational-specific post-shock relaxation models of air species of *ab-initio* accuracy that resolve both atom-molecule and molecule-molecule interactions. Particular emphasis is given to studying binary mixtures of pure oxygen and pure nitrogen in the temperature range 4,000-30,000K.

- Verify a new QCT sampling strategy for diatom-diatom collisional systems, in which only the first several low-lying vibrational quantum states are considered as a collisional partner.

- Assess the influence of atomic radicals in the collisional dynamics of a high-temperature gas.

- Validate the present models via numerical simulations of the shock-tube experiments of Sharma and Gillespie [10], Ibraguimova et al. [8], and Streicher et al. [7].

- Assess the assumptions and post-processing procedures made in each experiment. This includes Sharma and Gillespie's assumption that the excited electronic states of nitrogen are in vibrational equilibrium with its ground electronic state and Streicher et al.'s assumption that the relaxation behind the incident shocks may be assumed negligible to obtain the initial post-reflected shock conditions.

2. COMPUTATIONAL MODELING APPROACH*

At extreme hypersonic temperatures (above approximately 30,000K), the vibrational and rotational modes of O_2 and N_2 molecules exhibit similar relaxation times [34]. However, in general, the vibrational mode of a molecule will equilibrate on a time scale much larger than that of the rotational and translational modes and has a stronger coupling to chemical reactions, thus advocating for a thermo-chemical model's focus to be on vibration-dissociation coupling and vibrational state kinetics. This is the ideology followed in the present work.

While there are a host of models geared toward modeling thermal and chemical nonequilibrium, this work seeks to advance state-to-state modeling, which has its foundations in quantum mechanical principles. Although state-to-state modeling has become more prevalent in recent decades, MT models still carry the brunt of the workload in commercial applications due to their simplicity, ease of implementation, and cost-effectiveness. Recent advancements in processing power and efficient decoupled flow-chemistry formulations [35], however, provide the tools necessary to make state-resolved simulations in multiple dimensions and in the presence of multiple species feasible. Because of their prevalence, comparisons of the present state-to-state model predictions will be made to various MT models, and the shortcomings of such simplified models will be discussed.

2.1 Multi-temperature models

MT models are a reduced-order modeling strategy aimed at reproducing either shock-tube measurements [25] or results of higher-order numerical models, e.g. [36, 37]. Within the MT model framework, internal temperatures are used to describe the internal modes of the molecules. Because reduced-order models are typically designed to reproduce macroscopic parameters for a specific set of conditions, such as a post-shock environment, changes to the flow environment of-

*Reprinted with permission from "Vibrational-specific model of simultaneous N_2–N and N_2–N_2 relaxation under post-shock conditions", by A. J. Fangman and D. A. Andrienko, accepted for publication in *Journal of Thermophysics and Heat Transfer*, Copyright 2021 by Daniil A. Andrienko.

ten require additional experimental validation or revisiting the model of unreduced dimensions, as the original number of degrees of freedom has been reduced, and information has been lost.

Two MT approaches are used in this study for comparison with the vibrationally-resolved models: 1) Park's MT model [25], and 2) the Macheret-Fridman (MF) dissociation model [38]. The former is chosen because it is the most common method used for addressing thermo-chemical nonequilibrium, while the latter is chosen because it is physics-based (rather than phenomenological-based like Park's model) and can readily be applied to new interactions without having to fit rates to match previously computed data from another method. For both MT models implemented in this study, a separate vibrational temperature is assigned to each molecule. The equations which govern the transient thermal and chemical response in the MT models may be written as

$$\frac{\partial(\rho e_{vib})_M}{\partial t} = \rho_M \frac{e^*_{vib,M} - e_{vib,M}}{\tau_{vib,M}} + \dot{\omega}_M C_M^{DV} D_{e,M} \tag{2.1}$$

where the subscript M refers to the molecular species, and $e^*_{vib,M}$ refers to the average vibrational energy at the translational temperature, i.e. the average thermal equilibrium vibrational energy. The vibration-dissociation coupling coefficient, C_M^{DV}, determines the fraction of the dissociation energy which is gained/lost during recombination/dissociation and is model-dependent. C_M^{DV} is assumed constant for each molecule in Park's model, whereas it is temperature-dependent in the MF dissociation model. The vibrational relaxation time, $\tau_{vib,M}$, is computed as the harmonic-average of the vibrational relaxation times of all collisional partners

$$\frac{1}{\tau_{vib,M}} = \sum_s \frac{\chi_s}{\tau_{vib,M-s}} \quad \text{where} \quad \sum_s \chi_s = 1 \tag{2.2}$$

where the summation index s refers to the species considered. The individual relaxation times, $\tau_{v,M-s}$, are determined using the Millikan and White correlation [39] with Park's high-temperature correction [25]. The production terms, $\dot{\omega}_M$, are model-dependent. For Park's model, $\dot{\omega}_M$ is calculated using the global rates of Park [25], with a controlling temperature of $T_A = \sqrt{TT_v}$, and $\dot{\omega}_M$ is computed in the MF dissociation model according to Luo et al. [38] for the model which accounts

for rotational contributions. To be consistent with the master equation model, recombination rate coefficients are computed using the principle of detailed balance via partition functions at the translational temperature (recombining atoms are not dependent on the vibrational temperature).

2.2 Vibrational-specific state-to-state models

Vibrationally-resolved state-to-state models track the individual populations of each vibrational state of each molecule (N_2, O_2, and NO). Although previous studies employing state-resolved models relied on the FHO model [33] or SSH theory [40] for determining quantum state transition rates in 4-body collisions, rates of both atom-diatom and diatom-diatom transitions are computed using the Quasi-Classical Trajectory (QCT) method on Potential Energy Surfaces (PESs) of *ab-initio* accuracy in the present work, thus eliminating the uncertainties imposed by the analytic models. Because PESs have not yet been developed for non-adiabatic (i.e. multiple electronic state) transitions, all collisions are assumed to occur in each species' ground electronic state. Although this induces a small degree of uncertainty in the calculations, a majority of particles still reside in their ground electronic states. The discussion of non-adiabatic correction factors will be made throughout the text when appropriate (e.g. when discussing O_2, which has low-lying excited electronic states from which molecules may dissociate).

2.2.1 Quasi-classical trajectory method

The QCT method is used to describe energy redistribution in collisions of air molecules (O_2, N_2, or NO) with other air species (O, N, O_2, N_2, or NO). Billions of collision trajectories between target molecules and projectile species on high-fidelity PESs are used to generate probabilities of occurrence for specific quantum-state transitions. These probabilities are then post-processed to obtain cross-sections and, subsequently, rate coefficients for each transition. Further details on the QCT method and the post-processing of cross-sections may be found elsewhere [41].

Because the number of QCT trajectories required to resolve all possible transitions in a diatom-diatom collision is extremely computationally expensive, several simplifications are made to reduce the cost of the diatom-diatom QCT sampling — the accuracy of which will be verified. First,

translational-rotational equilibrium is assumed. Accuracy of this assumption for the temperature range of interest is rigorously assessed through comparisons with the Direct Molecular Simulation (DMS) method [4, 6], which does not assume translational-rotational equilibrium. Second, transitions are calculated assuming all collisions are induced by projectile molecules in the first several low-lying vibrational states, while target molecules are allowed to occupy any of the vibrational states. This assumption is based on the idea that a majority of molecules reside in low vibrational states and that the projectile molecule's internal energy is not as influential in determining the outcome of a collision event as the target molecule's internal energy. The latter point is reinforced for dissociation by Chaudhry et al.'s [42] presentation of a support factor, which characterizes the influence of the projectile and target molecules' internal energies on the result of dissociative collision events. Although Chaudhry et al. show that the probability of dissociation is weakly dependent on the projectile molecule's internal energy, they do not study its influence on bound inelastic collisions, thus a convergence study was completed to determine whether simulating collisions with molecules in only low-lying vibrational states is representative of the full diatom-diatom system for both excitation and dissociation. The results of this convergence study for the N_2–N_2 collisional system are detailed in Appx. A.

While an overview of the entire QCT air database may be found in [43], an additional description should be given to the binary mixture database, since it is used heavily throughout this work. Both N_2–N_2 and N_2–N rate coefficients are computed using the singlet N_4 PES constructed at the University of Minnesota (UMN) [44]. This PES was generated using both N_2–N_2 and N_2–N atomic geometrical arrangements; therefore, rate coefficients for the latter can be obtained by displacing one of the nitrogen atoms to infinity in the QCT trajectories, such that its influence on the interaction is nullified. O_2–O rate coefficients are taken from Andrienko [1], who employed all nine spin-spatial degenerate PESs corresponding to the ground state interactions. While there are three PESs of different spin-spatial degeneracy that correspond to adiabatic collisions of O_2–O_2 in the ground electronic state, the current work uses only the triplet surface proposed by Paukku et al. [45]. This choice builds on prior O_2–O_2 QCT dissociation calculations [46], which used the triplet

O_4 PES proposed by Varandas et al. [47], as it was the only one available at the time. Moreover, for the purposes of this work, using only the triplet PES is a reasonable first assumption, as macroscopic quantities derived from each surface have previously been shown to be comparable [48, 49]. Because only the triplet PES is used, no statistical weight is applied to the O_2–O_2 rate coefficients (i.e. the spin-spatial degeneracies of 1/9, 3/9, and 5/9 for the singlet, triplet, and quintet surfaces, respectively, are not applied).

2.2.2 Rate coefficient temperature interpolations

Curve fits must be constructed to bridge the temperature gaps in the QCT-generated rate coefficients. This allows for their use in the adiabatic reservoir and normal shock simulations discussed in Section 3. Dissociation rate coefficients are fitted to a modified Arrhenius expression

$$D_v^{sys}(T) = \exp(A_v^{sys}) T^{B_v^{sys}} \exp\left(\frac{-C_v}{T}\right) \tag{2.3}$$

where the superscript sys refers to the collisional system, and A, B, and C are the state-specific interpolation constants. C_v is defined as the difference between the classical dissociation energy of the dissociating molecule and the energy of its current vibrational state.

Bound-bound rate coefficients of vibrational-translational (VT) energy transfer are fitted to a form similar to that employed by Esposito et al. [50] for O_2–O QCT studies

$$K_{v\to v'}^{sys}(T) = \quad 10^{-14} \times \exp\left(\alpha_{v,v'}^{sys} + \frac{\beta_{v,v'}^{sys}}{\ln(T)} + \gamma_{v,v'}^{sys} \times \ln(T) + \delta_{v,v'}^{sys} \times \big(\ln(T)\big)^2\right) \tag{2.4}$$

where α, β, γ, and δ are the state-specific interpolation constants.

To determine the state-specific interpolation constants, MATLAB's built-in non-linear regression tools are used (although an alternative approach would be to linearize the rate coefficients in terms of the unknown interpolation constants by taking the natural logarithm of the fit expression, then using a method such as least squares to obtain the constants). Plots of global equilibrium dissociation rate coefficients and vibrational relaxation times (discussed in detail in Section 3.1) using

the exact rate coefficients computed in the QCT analysis and with the fitted rate coefficients are provided in Fig.'s 2.1 and 2.2 for pure nitrogen interactions to show that the macroscopic quantities derived using the fits are consistent with the exact QCT data.

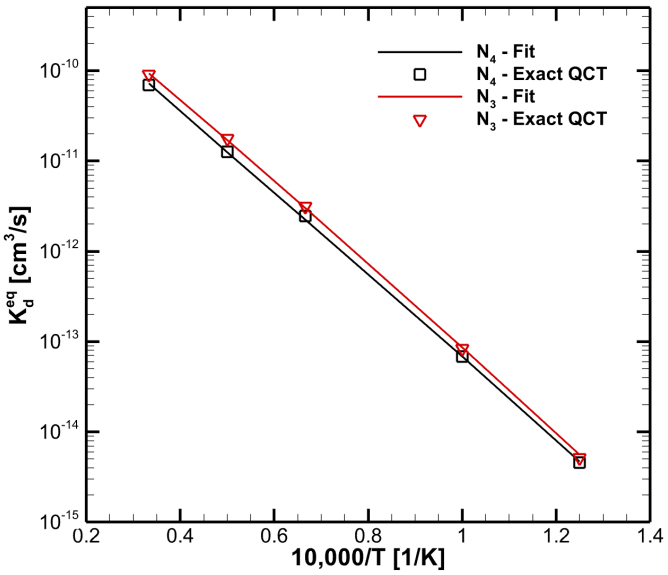

Figure 2.1: N_2–N_2 and N_2–N equilibrium dissociation rate coefficients using fitted and exact QCT rate coefficients.

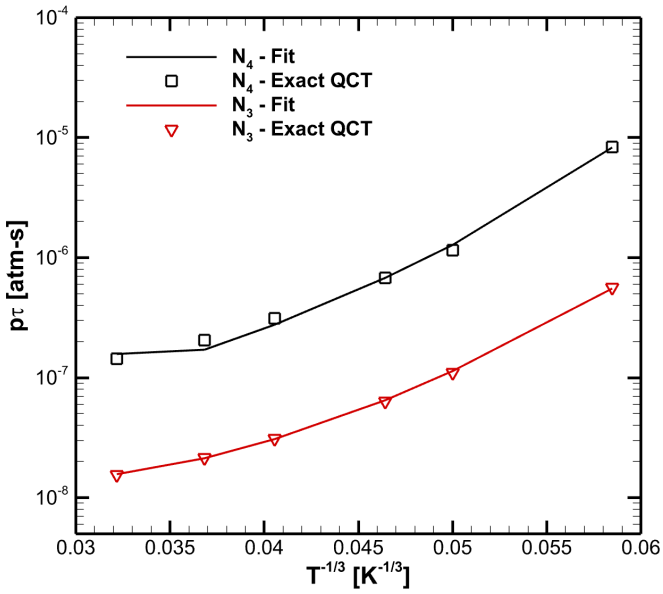

Figure 2.2: N_2–N_2 and N_2–N vibrational relaxation times using fitted and exact QCT rate coefficients.

2.2.3 Master equations

The transient thermo-chemical state of a relaxing system can be obtained by implementing QCT kinetic database into a coupled set of differential equations, referred to as the master equations (MEs), which track the individual vibrational state number densities. For a non-ionizing binary mixture of either pure oxygen or pure nitrogen, the MEs may be written as

$$\frac{dn_v^M}{dt} = \sum_P \left(\sum_{v \neq v'} \left(K_{v' \to v}^{M-P} n_P n_{v'} - K_{v \to v'}^{M-P} n_P n_v \right) + R_v^{M-P} n_P n_A^2 - D_v^{M-P} n_P n_v, \right) \quad (2.5)$$

where the superscript M refers to the molecule (N_2 or O_2), the subscript A refers to the atom (N or O), the summation index P refers to the possible projectiles (O and O_2 for pure oxygen mixtures and N and N_2 for pure nitrogen mixtures), and R_v^{M-P} designates the recombination rate coefficients to vibrational state v as a result of three-body collisions. Only vibrational-translational energy transfer and single dissociation events are considered in this work, as vibrational-vibrational

energy transfer and double dissociation events (i.e. collisions where two molecules dissociate simultaneously) are negligible for the hypersonic temperatures of interest in this work. Because bound-bound exothermic transitions ($v > v'$) have better accuracy in the QCT calculations — due to their increased probability of occurrence — endothermic bound-bound rate coefficients are obtained through the principle of detailed balance. The amount of atomic species can be found either through total nuclei balance or via summation of Eq. 2.5 for all v and v', recognizing that bound-bound transitions do not change atomic concentrations.

For the full 5-species air model, the additional possible collisional partner terms must be added to Eq. 2.5, and conservation equations for the vibrational states of NO must be considered. This formulation is not written here, as it cannot be written compactly due to the Zel'dovich exchange mechanisms (see Ref. [43] for the full formulation). Additionally, because high-fidelity PESs have not yet been developed for collisions of nitric oxide with other molecules, and the influence of these molecule-molecule collisions is likely minimal compared to those with atomic partners, interactions of NO with NO, O_2, and N_2 are not considered in the present model when simulating the 5-species air system.

2.2.4 Rovibrational energy ladders and the calculation of internal energies

It is important to note that interpolation across energy ladders is unavoidable when constructing a state-resolved model of air [51]. All binary mixtures simulated in this work are done so using the original rate coefficients on their original rovibrational ladders (i.e. the 55 and 44 vibrational state N_2 and O_2 energy ladders of the UMN PESs obtained from the Wentzel–Kramers–Brillouin method). However, when the full 5-species air system is simulated, the rate coefficients computed on PESs with different energy ladders are scaled onto a common vibrational energy ladder. Care is taken to minimize this interpolation error.

To compute vibrational and rotational energies, the vibration-prioritized framework is used — that is, the vibrational energy of a rovibrational state with a vibrational quantum number v and a rotational quantum number j is defined as $\epsilon_{v,j=0}$, and the rotational energy is defined as $\epsilon_{v,j} - \epsilon_{v,j=0}$.

2.2.5 Limitations of the present vibrational-specific model

As with any numerical model, it is important to address its limitations and range of applicability. The present vibrational-specific model is intended to accurately predict post-shock conditions in a non-ionizing 5-species air mixture in the temperature range 5,000-30,000 K. Above this temperature, the rotational relaxation times of air molecules become comparable to their vibrational relaxation times [34], which might change dissociation characteristics of the flow. Additionally, electronic excitation and radiation of air species become increasingly important at high temperatures, which provide additional channels of energy relaxation [52].

Nevertheless, the present model is applicable for a wide range of hypersonic conditions. Unlike combustion modeling — where hundreds, or even thousands of reactions may be necessary to capture the state of the gas [53] — the 5-species air system is able to capture the dominant flow field physics for a number of hypersonic applications: ranging from external flow around trans-atmospheric air-breathing vehicles, to the extreme post-shock environments experienced during the entry and descent phases of reentry capsules [54]. Furthermore, an advantage of the master equation approach is that it is straightforward to add additional species and excited electronic states to the model if necessary; although appropriate PESs must be generated first, which may be a non-trivial task. Recent advances in machine learning have shown promise in providing the tools necessary for developing these PESs in an accurate and efficient manner [55].

2.3 Post-shock relaxation simulations

The following subsections provide an outline of the methodology and basic equations implemented to numerically simulate various post-shock conditions. First, a synopsis of idealistic 0-D isothermal and adiabatic reservoir cases is provided, from which global parameters will be extracted and compared to the existing experimental and computational results. Next, 1-D incident shock modeling is detailed, with an emphasis on making comparisons to Ibraguimova et al.'s [8] shock-tube experiments. Finally, the numerical modeling of 1-D reflected shocks is discussed, as one of the goals of this work is to analyze the recent shock-tube experiments of Streicher et al. [7].

2.3.1 0-D isothermal reservoirs

Isothermal reservoirs provide an opportunity to extract and compare ensemble-averaged parameters, such as vibrational relaxation times and dissociation rate coefficients under thermal equilibrium and nonequilibrium conditions. The transient thermo-chemical state of such a system is determined by integrating the MEs (e.g. Eq. 2.5 if a binary mixture is considered) forward in time from an initial nonequilibrium state. For a vibrational-specific model, the translational-rotational temperature is forced to remain constant while the vibrational mode relaxes toward thermal equilibrium. In this work, the vibrational temperature is defined as the temperature at which a Boltzmann distribution of vibrational states reproduces the instantaneous average vibrational energy of the system.

Although isothermal reservoir calculations are a valuable tool for assessing a thermo-chemical nonequilibrium model, it is important to stress that conclusions drawn from comparisons of macroscopic properties, such as compositions, between various isothermal models that rely on different underlying assumptions of internal energy modes should be made with caution. The present vibrational-specific model assumes that the rotational mode instantaneously achieves and maintains full equilibrium with the translational mode. This implies that the energy flux necessary to keep a constant translational-rotational temperature is not equal to the energy flux required to keep a constant translational temperature in an isothermal model constructed by means of a rovibrational method, such as the DMS method, in which no such assumption of translation-rotational equilibrium is made. The adiabatic reservoir calculation, however, provides a base for such one-to-one comparisons, as the energy flux is set to zero in all models. In a real post-shock flow, the kinetic energy associated with the mean motion of the gas is gradually converted to internal energy, thus the isothermal and adiabatic reservoirs may be viewed as limiting cases on the actual relaxation toward equilibrium.

2.3.2 0-D adiabatic reservoirs

In an adiabatic reservoir, the total energy — which is a sum of the translational, rotational, vibrational, and chemical contributions — is fixed. This implies the gas translational temperature is no longer constant. As energy is redistributed between the translational and other internal modes, and as endothermic dissociation processes occur, the gas temperature drops. Aside from any bulk kinetic energy contribution and transport phenomena, this system has strong similarities to the conditions experienced in post-normal shock environments. The total energy per unit volume for a non-ionizing gas mixture can be written as

$$E_{tot} = \underbrace{\sum_{s} \frac{3}{2} n_s k_b T}_{\text{Trans. Energy}} + \underbrace{\sum_{M} \sum_{v} n_v^M \epsilon_{v,j=0}^M}_{\text{Vib. Energy}} + \underbrace{\sum_{M} \sum_{v} \sum_{j \in v} \frac{n_v^M Q_j^M(T)(\epsilon_{v,j}^M - \epsilon_{v,j=0}^M)}{\sum_j Q_j^M(T)}}_{\text{Rot. Energy}} + \underbrace{\sum_{s} n_s h_{f,s}^\circ}_{\text{Chem. Energy}} \tag{2.6}$$

where the summation index s refers to any species (N, O, N_2, O_2, or NO), the summation index M refers to any molecular species (N_2, O_2, or NO), and $h_{f,s}^\circ$ is the chemical formation enthalpy of species s. $Q_j^M = g_s(2j+1)exp(-\epsilon_{v,j}/k_b T)$ is the rovibrational Boltzmann factor, where the nuclear spin degeneracy, g_s, differs for odd and even rotational states. For O_2, g_s is 1 for odd rotational states and 0 for even rotational states. For N_2, g_s is 3 for odd rotational states and 6 for even rotational states (per convention, these are normalized to 1/3 and 2/3 [56]). For the heteronuclear molecule NO, g_s is always 1.

The vibrational state number densities, n_v, are determined from the solution of the master equations (e.g. Eq. 2.5 if a binary mixture is considered). After each integration time step, the translational temperature is updated using Eq. 2.6 by solving a root-finding problem. The rotational and translational energies are not known *a priori*; however, the rotational states are assumed to follow a Boltzmann distribution at the translational temperature. A typical simulation of an adiabatic reservoir using the present vibrational-specific ME model takes approximately 2 core-min.

2.3.3 1-D incident shocks

To model the post-incident shock relaxation in Ibraguimova et al.'s oxygen [8] and Sharma and Gillespie's [10] nitrogen experiments, the set of master equations, given by Eq. 2.5, are coupled with the species, momentum, and energy conservation laws for an inviscid flow. Because the incident shock-wave is assumed to have a constant velocity, u_{is}, this formulation can be written in the shock frame of reference as

$$\frac{\partial}{\partial x}\begin{pmatrix} n_O u \\ n_v u \\ p+\rho u^2 \\ h+\rho u^2/2 \end{pmatrix} = \begin{pmatrix} \partial n_O/\partial t \\ \partial n_v/\partial t \\ 0 \\ 0 \end{pmatrix}, \quad v = \begin{cases} 0,...,43 & \text{if } O_2 \\ 0,...,54 & \text{if } N_2 \end{cases} \tag{2.7}$$

where p is the total pressure, ρ is the mass density, u is the mean velocity of the flow, and h is the internal enthalpy. The conversion between temporal and spatial derivatives is made through the relationship $dx = udt$. The incident shock-wave velocity is assumed constant; therefore, the mean velocity in the shock frame, u, may also be written as $u = u_{is} - u_2$, where u_2 is the post-incident shock velocity in the laboratory frame. The integration is treated as an initial value problem, and initial conditions directly behind the shock front are determined using the Rankine-Hugoniot relations, where it is assumed that the vibrational and chemistry modes are frozen through the shock.

2.3.4 1-D reflected shocks

Reflected shocks are advantageous for studying high-temperature chemical kinetics, as they are capable of producing high-temperature nonequilibrium test gas under nearly stagnated conditions. To avoid complications that arise upon the interaction of the reflected shock and boundary layer, such as the bifurcation process [57], measurements are taken close to the end wall. Reflected shock experiments have been employed to deduce a wealth of high-temperature data, including vibrational relaxation times [58, 7], chemical reaction and combustion rates [59], and dissociation

energies [60]. Recently, Streicher et al. [7] performed measurements of vibrational temperature behind shocks in O_2–Ar and pure O_2 mixtures by employing a strategy similar to that of Ibraguimova et al. [8]. The new element of the former work was to use two UV lasers simultaneously, allowing for a substantial reduction of uncertainty. As in the work by Ibraguimova et al., translational temperature and composition profiles were then derived by invoking energy and mass conservation laws.

To numerically model the reflected shock experiments by Streicher et al. [7], a modified version of the methodology by Hanquist et al. [61] is implemented, in which the unsteady nature of the reflected shock is approximated by 'stitching together' the solutions of multiple steady-state shock calculations. Unlike Hanquist et al., however, an attempt is made to account for the varying reflected shock velocity between the end wall and observation location. As vibrational relaxation and endothermic dissociation processes occur behind the reflected shock, density increases, and rarefaction waves are generated in order to satisfy the conservation of mass, momentum, and energy laws. These waves weaken the reflected shock and cause the shock front's velocity to decrease.

In contrast to Hanquist et al., who assumed a constant reflected shock velocity from the wall to the measurement location, a third steady-state shock calculation is used here to approximate the reflected shock's unsteady characteristics. An overview of the shock solution procedure implemented is thus as follows (the common delineation of shock-tube regions is followed, i.e. regions 1, 2, and 5 correspond to the undisturbed fill gas, post-incident shock, and post-reflected shock conditions, respectively). Again, all calculations are made in either the incident or reflected shock frame of reference, as indicated.

1. Provide an initial estimate for the particle time that elapses between the passage of the incident shock and the point at which the shocked gas is stagnated at the measurement location by the passage of the reflected shock, t_e^0 (i.e. similar to Hanquist et al., region 5 fluid motion is not considered).
2. Solve the Rankine-Hugoniot relations for the incident shock using the specified fill pressures

and shock velocities recorded in the experiment to find the initial region 2 pressure, translational temperature, and post-shock velocity. Composition and the vibrational mode are assumed frozen through the shock front.

3. Integrate the Euler equations (Eqs. 2.7) from $t = 0$ to $t = t_e^0$, where time, t, and displacement from the incident shock front, x, are related through the relation $dt = dx/(u_{is} - u_2)$. Again, u_{is} and u_2 are the incident shock and post-incident shock velocities in the laboratory frame, respectively.
4. Solve the Rankine-Hugoniot relations directly at the end wall to obtain the initial pressure, translational temperature, and reflected shock velocity at the wall. Composition and the vibrational mode are assumed frozen (see Section 7.3 of Anderson [62] for further details).
5. Integrate the Euler equations (Eqs. 2.7) using the initial conditions at the end wall until the measurement location distance, d, is reached (5mm for the cases considered in this study).
6. Obtain the actual t_e based on the results of steps 3 and 5. This may be written mathematically as: $t_e = \int_0^{t_e^0} \frac{u_2(t)dt}{u_{is}} + \frac{d}{u_{is}} + \int_0^d \frac{dx}{u_{rs}(x)}$, where u_{rs} is the reflected shock velocity in the laboratory frame.
7. Update t_e^0 and repeat steps 3-6 until t_e^0 is equal to t_e from step 6 within a specified convergence. The convergence criteria chosen is $|t_e - t_e^0| \leq 0.01$ μs, which implies that the guessed elapsed time is well within 1% of the computed elapsed time, as typical t_e are $\mathcal{O}(50\mu s)$ for the cases considered in this study.
8. Solve the Rankine-Hugoniot relations to find the initial region 5 pressure, translational temperature, and vibrational temperature using the relaxed, nonequilibrium region 2 translational temperature, vibrational temperature, pressure, and velocity at the measurement location as the upstream conditions, which are obtained in step 3 after t_e. The upstream velocity as seen by the reflected shock is $u_{rs} + u_2$, where u_2 and u_{rs} are obtained in steps 3 and 5, respectively. Composition and the vibrational mode are assumed frozen through the shock front.
9. Integrate the Euler equations (Eqs. 2.7) to determine the final time-histories of the vari-

ables of interest in region 5 at the measurement location, where time is obtained through the relation $dt = dx/u_{rs}$.

A caveat must be accounted for in the implementation of the steady-state Euler equations in the reflected shock frame in steps 5 and 9: the deceleration of the reflected shock. Newton's second law must be applied for an acceleration that is relative to an inertial (laboratory) reference frame. Because u_{rs} decreases as the flow relaxes behind the wave, the momentum equation must be modified to account for the shock as a non-inertial frame of reference. The governing equations for the reflected shock therefore become:

$$\frac{\partial}{\partial x}\begin{pmatrix} n_O u_{rs} \\ n_v u_{rs} \\ p + \rho u_{rs}^2 \\ h + \rho u_{rs}^2/2 \end{pmatrix} = \begin{pmatrix} \partial n_O/\partial t \\ \partial n_v/\partial t \\ \rho a_{rs} \\ 0 \end{pmatrix}, \quad v = \begin{cases} 0, ..., 43 & \text{if } O_2 \\ 0, ..., 54 & \text{if } N_2 \end{cases} \tag{2.8}$$

where a_{rs} is the acceleration of the reflected shock. The sign of the right-hand side of the momentum equation is flipped from the conventional treatment of a non-inertial frame of reference [63] because a_{rs} is computed as part of the integration of the Euler equations (Eqs. 2.8) in the shock frame as $\partial u_{rs}/\partial t$. The computed a_{rs} will point in the opposite direction of the acceleration of the reflected shock in the laboratory frame.

It is assumed that the velocity of the test gas behind the reflected shock is instantaneously stagnated in the laboratory frame, such that the post-shock velocity in the reflected shock frame is the shock velocity itself, u_{rs}. Additionally, under the assumption that a_{rs} can be expressed as $\partial u_{rs}/\partial t$, the region 5 pressure will remain constant; this can be verified through manipulation of the mass and momentum conservation laws as follows.

The acceleration of the reflected shock may be expressed as

$$a_{rs} = \frac{\partial u_{rs}}{\partial t} = u_{rs}\frac{\partial u_{rs}}{\partial x} \tag{2.9}$$

By writing the momentum equation in terms of pressure and using Eq. 2.9, the momentum equation becomes

$$\frac{\partial p}{\partial x} = \rho u_{rs} \frac{\partial u_{rs}}{\partial x} - \frac{\partial (\rho u_{rs}^2)}{\partial x} \tag{2.10}$$

The second term may then be expanded and the conservation of mass applied.

$$\frac{\partial p}{\partial x} = \rho u_{rs} \frac{\partial u_{rs}}{\partial x} - \left(u_{rs} \cancelto{0}{\frac{\partial (\rho u_{rs})}{\partial x}} + \rho u_{rs} \frac{\partial u_{rs}}{\partial x} \right) \tag{2.11}$$

The first and the third terms on the right-hand side of Eq. 2.11 cancel, implying that the region 5 pressure will remain constant in the present model.

$$\frac{\partial p}{\partial x} = 0 \tag{2.12}$$

Although the region 5 pressure typically rises in reflected shock-tube experiments as the system relaxes toward equilibrium and as non-ideal processes occur (which themselves incur a corresponding temperature increase through the isentropic relations [64]), pressure is much less sensitive to departures from equilibrium than temperature and density [58]. Therefore, the influence of including the non-ideal pressure increases reported in experimental studies is likely of secondary importance, thus it is not considered in the present reflected shock numerical model.

Because the numerical model does not continue to account for relaxation in region 2 after determining the initial conditions for the Rankine-Hugoniot relations for the reflected shock at the measurement location, the acceleration of the shock front due to this relaxation and the final equilibrium shock velocity obtained will not correspond to the true solution. However, the characteristic times for vibrational excitation and dissociation in region 2 are much smaller than those in region 5, and the deviations from equilibrium are much smaller, implying that the influence of continued relaxation in region 2 on the region 5 time-histories is likely minimal in the time windows of interest.

3. RESULTS AND ANALYSIS*

3.1 Ensemble-averaged dissociation rates and vibrational relaxation times

The following two subsections present the QCT-computed thermal equilibrium and Quasi-Steady State (QSS) dissociation rate coefficients and vibrational relaxation times for the N_2–N_2 and O_2–O_2 collisional systems.

Equilibrium dissociation rate coefficients are computed by averaging the state-specific rate coefficients over a Boltzmann distribution of vibrational states at a given translational-rotational temperature. Although thermal equilibrium dissociation rate coefficients provide a high-level sense of a model's dissociative characteristics, dissociation at hypersonic temperatures more often occurs through transient quasi-steady states, in which a balance is struck between the dissociation of molecules from upper vibrational states and the repopulation of these states due to excitation processes. This results in a nearly constant internal energy distribution, which is characterized by depleted upper vibrational states. For a given translational-rotational temperature, a QSS dissociation rate coefficient may be determined by setting the left-hand side of the master equations (Eq. 2.5) to zero, solving the resulting set of algebraic equations, and using this QSS vibrational state distribution to compute a global dissociation rate coefficient [65]. Vibrational relaxation times are computed from isothermal reservoir simulations using the e-folding method [66].

3.1.1 N_2–N_2

N_2–N_2 thermal equilibrium dissociation rate coefficients are shown in Fig. 3.1. Present calculations are in good agreement with previous computational results, including the QCT rates of Bender et al. [44] and the vibrational-based Coarse-Grained (CG) grouping method rates of Macdonald et al. [67]. While Bender et al. computed their results on the same UMN PES used in

*Reprinted with permission from "A state-to-state and multi-temperature study of air thermochemistry" by A. J. Fangman and D. A. Andrienko, 2021. *AIAA Scitech 2021 Forum*, p. 0316, Copyright 2021 by American Institute of Aeronautics and Astronautics, Inc., and from "Vibrational-specific model of simultaneous N_2–N and N_2–N_2 relaxation under post-shock conditions", by A. J. Fangman and D. A. Andrienko, accepted for publication in *Journal of Thermophysics and Heat Transfer*, Copyright 2021 by Daniil A. Andrienko.

this work, Macdonald et al. employed the NASA Ames N_4 surface [68]. Irrespective of this, close agreement is observed between the two surfaces. Grover et al. [69] noted similar findings between the NASA Ames [70, 71] and Minnesota surfaces for the N_2–N system. Although it is known that the Ames and Minnesota N_4 PESs have different long-range behaviors and channel energy barriers, macroscopic properties from the two sets of surfaces have been shown to be comparable [72].

All computational models tend to overpredict the experimental data, which includes that of Appleton et al. [58] and Kewley and Hornung [73]. At high temperatures (greater than approximately 10,000 K for nitrogen), dissociation tends to occur while the system is in a QSS, where thermalization of the internal modes is not yet complete, and the vibrational energy distribution is characterized by a depleted tail. This is likely why lower dissociation rates are observed by the experiments.

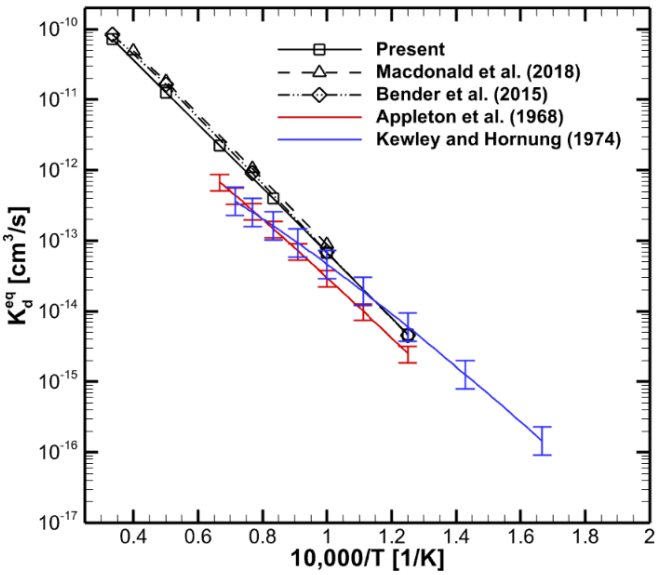

Figure 3.1: N_2–N_2 equilibrium dissociation rate coefficients.

Fig. 3.2 shows the present QSS dissociation rate coefficients alongside the same experimental results of Appleton et al. and Kewley and Hornung, the vibrational CG-grouping method predictions of Macdonald et al., and the DMS method predictions of Grover [74]. Again, the agreement

between the present results and the other computation ones is good. The computational QSS dissociation rates are in better agreement with the experimental curve fits than the equilibrium rates, particularly for temperatures larger than approximately 10,000K, for which they fall within the reported experimental error bounds.

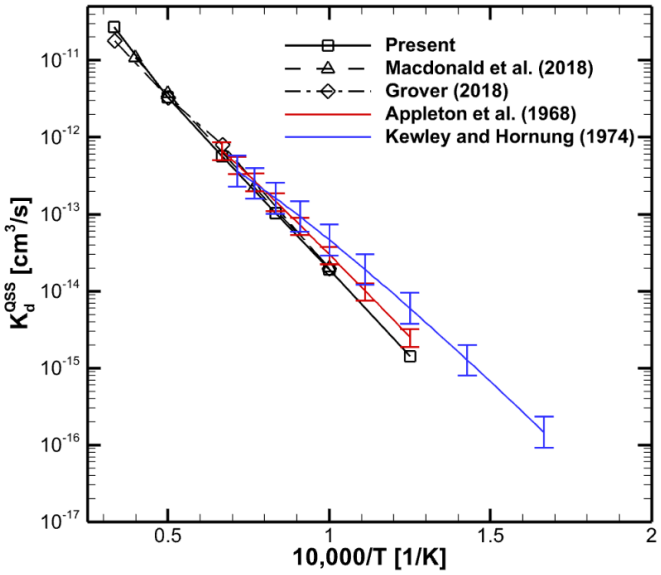

Figure 3.2: N_2–N_2 QSS dissociation rate coefficients.

Fig. 3.3 compares the present N_2–N_2 vibrational relaxation times with the DMS method predictions of Valentini et al. [2], the vibrational-based CG grouping method predictions of Macdonald et al. [67], the experimental data of Appleton [58], and the Millikan and White correlation [39] with Park's high-temperature correction [25]. The high-temperature correction is applied to the Millikan and White correlation to ensure the predicted vibrational relaxation times do not become smaller than the average elastic collision time; this correction is dependent on the average molecular speed, number density, and a collision limiting cross-section, σ_v. Two values for the collision limiting cross-section, σ_v, in the high-temperature correction are shown in Fig. 3.3: 1) the commonly used expression $3\times10^{-17}(50,000/T)^2$ cm^2, and 2) the constant 3×10^{-18} cm^2 value used by Kim in Boyd [9] in their 1-D post-shock simulations of Sharma and Gillespie's shock-tube

experiment. The choice of the high-temperature correction results in approximately an order of magnitude difference in the vibrational relaxation times — this is demonstrated to be important in the numerical simulations of Sharma and Gillespie's experiment, which are discussed in Section 3.4.3.

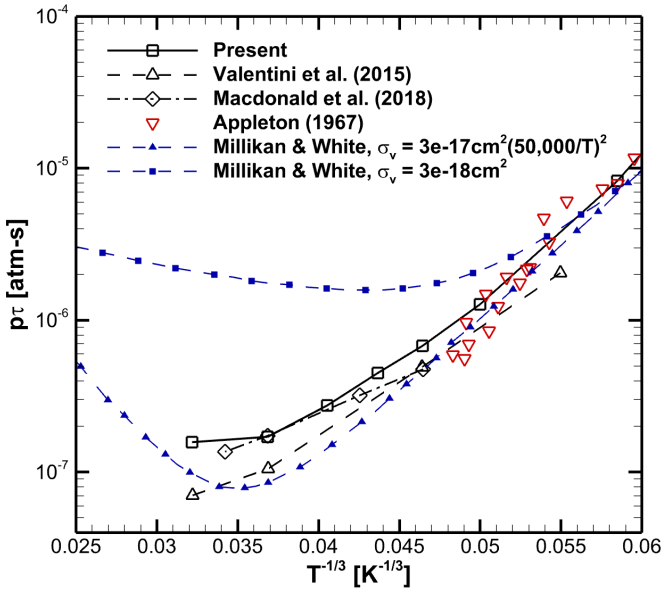

Figure 3.3: N_2–N_2 vibrational relaxation times.

The present vibrational relaxation times are in good agreement with the Millikan and White correlation at low temperatures and fall within the experimental spread of Appleton et al. Although the present results and those of Macdonald et al.'s vibrational-based CG method are computed on different PESs, close agreement is again observed between the two.

In comparison to the DMS method calculations of Valentini et al., the present model predicts somewhat slower relaxation, with differences becoming larger at higher temperatures. This observation of slower relaxation times at higher temperatures for a vibrational-based grouping model of the N_2–N_2 system was also observed by Macdonald et al. [75] and may be a result of the non-optimal grouping strategy hindering thermalization between close energy states with different vibrational quantum numbers.

3.1.2 O_2–O_2

Fig. 3.4 compares the O_2–O_2 thermal equilibrium dissociation rate coefficients against previously published data, including the QCT-derived rate coefficients of Andrienko et al. [46] and Chaudhry [76], the FHO-derived rate coefficients of da Silva et al. [77], Streicher et al.'s [7] experimental best fit, and the experimental measurements of Shatalov [78].

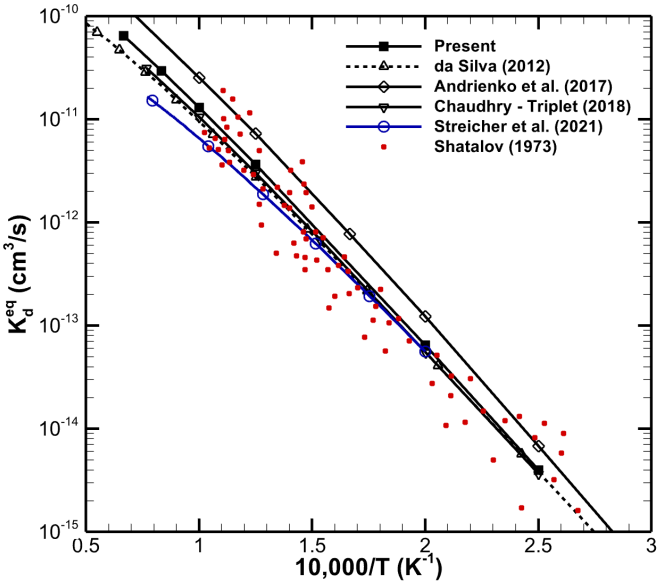

Figure 3.4: O_2–O_2 equilibrium dissociation rate coefficients.

The present equilibrium dissociation rate coefficients lie within the experimental uncertainty reported by Shatalov and show good agreement with Chaudhry's (triplet surface) and da Silva et al.'s computational results. The overestimation of Andrienko et al.'s rate coefficients in Fig. 3.4 is a consequence of using different PESs, indicating that Varandas et al.'s O_4 PES [47] is more dissociative than Paukku et al.'s [45].

O_2–O_2 QSS dissociation rate coefficients are presented in Fig. 3.5 alongside the (nonequilibrium) experimental spread of Shatalov [78], the QCT-derived results of Andrienko et al. [46], and the DMS method results of Grover et al. [48]. Andrienko et al. used the FHO model to determine

the relevant bound-bound transition rate coefficients to determine the QSS rates. Grover et al. employed all three PESs corresponding to adiabatic collisions of O_2–O_2 in the ground electronic state, hence their profile is labeled 'Full O_4' in the figure.

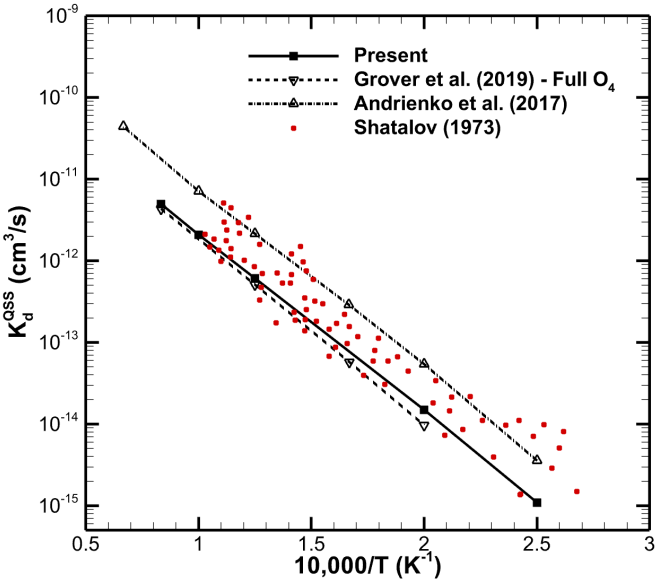

Figure 3.5: O_2–O_2 QSS dissociation rate coefficients.

The present QSS dissociation rate coefficients fall within Shatalov's experimental spread; however, they are nearly half an order of magnitude lower than those reported by Andrienko et al. — this difference reflects the differences already noted between the two PESs. The present K_d^{QSS} agree well with those predicted by Grover et al, implying that dissociation from the triplet surface is representative of the full O_4 system to a first approximation. It should be noted that while the original publication of Grover et al. uses the non-adiabatic multiplication factor, η = 16/3, it is presented here without it. The decision by Grover et al. to apply η appears to originate from an unbalanced comparison of the DMS method nonequilibrium dissociation rate coefficients to equilibrium dissociation rate coefficients from experiments. The unbalanced comparison resulted in requiring the use of η to better fit the experimental measurements. However, when K_d^{QSS} is correctly compared to nonequilibrium dissociation results from experiments, it is found that there is

no need for the non-adiabatic correction factor. Andrienko et al. and Chaudhry [76] also came to this conclusion for the O_2–O_2 system.

The computed characteristic O_2–O_2 vibrational relaxation times are shown in Fig. 3.6 alongside the DMS method predictions of Grover et al. [48], the Millikan and White correlation [39], and the experimental results of Ibraguimova et al. [8] and Streicher et al. [7]. The O_2–O vibrational relaxation times of Andrienko [1] are also plotted.

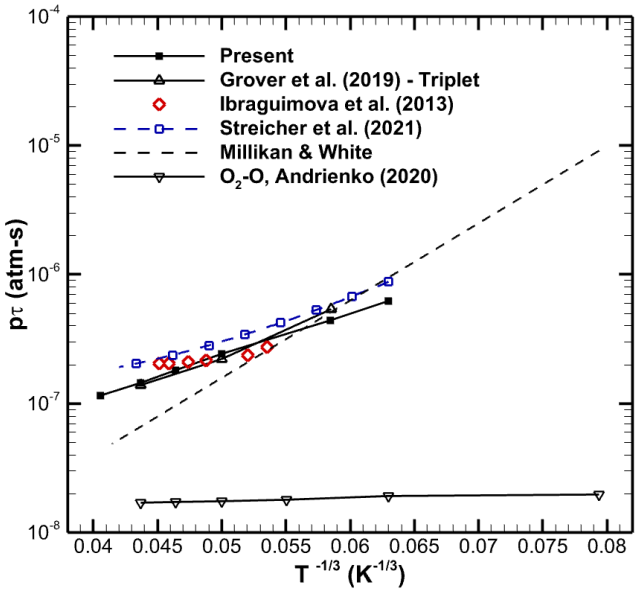

Figure 3.6: O_2–O_2 vibrational relaxation times. O_2–O vibrational relaxation times of Andrienko [1] are also plotted.

Although the present results are in good agreement with Grover et al.'s DMS method results on the triplet surface, they underestimate the most recent experimental results of Streicher et al. These shock-tube experiments are numerically simulated in Section 3.4.1 to help shed light on the discrepancies between model and experiment. All models predict much slower relaxation times than those of the Millikan and White correlation at high temperatures. Unlike O_2–O_2, there is a weak dependence of O_2–O relaxation times on temperature. The O_2–O relaxation times are also more than an order of magnitude faster than the O_2–O_2 relaxation times at all temperatures, im-

plying that the O_3 collisional system is considerably more effective in vibrational energy exchange than the O_4 collisional system. This fact will become important in understanding the results of the adiabatic post-shock simulations in the following sections.

3.2 The influence of atomic radicals on high-temperature collisional dynamics

Insight into the collisional dynamics of a molecular system can be obtained by studying populations of individual internal energy states and the probabilities with which these states dissociate. Because dissociation at hypersonic temperatures often occurs through transient quasi-steady states (QSS), in which a balance is struck between the preferential dissociation of molecules from upper vibrational states and the repopulation of these states due to excitation processes, interesting physics can be obtained by analyzing QSS vibrational state distributions.

The QSS vibrational state distributions extracted from isothermal reservoir simulations at 10,000, 20,000, and 30,000K are shown in Fig.'s 3.7-3.9, respectively. Again, a non-ionizing nitrogen mixture is considered for simplicity. The vibrational-specific ('Present') model predictions are shown for two cases: 1) considering both N_2–N_2 and N_2–N interactions, denoted 'Mixture' in the figures (square symbols), and 2) considering only N_2–N_2 interactions, denoted 'N_4 only' in the figures (gradient symbols). Also shown are results of previously reported DMS method data [2, 3]. It is important to note that the same PES has been used in both the DMS method and the vibrational-specific model calculations. The DMS method does not decouple internal energy modes, which provides a means for addressing the assumption of translational-rotational equilibrium made in the present vibrational-specific model.

When both N_2–N_2 and N_2–N interactions are considered, good agreement is observed between the vibrational-specific model QSS predictions and those of the DMS method for all temperatures. However, when N_2–N collisional dynamics are excluded from the analysis, noticeable differences can be seen near the tails of the vibrational state distributions, where the present vibrational-based grouping model predicts a greater depletion of high energy states. This artifact is likely primarily due to the assumption of translational-rotational equilibrium and the less efficient energy redistribution in N_2–N_2 collisions. These observations become apparent when analyzing the dissoci-

ation probability density functions (PDFs), which define the pre-collision states of dissociating molecules.

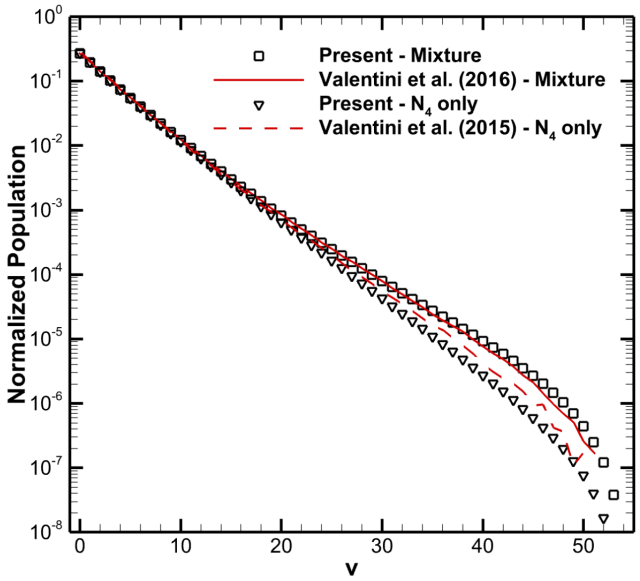

Figure 3.7: Comparison of QSS vibrational distributions between the present vibrational-based grouping model and the DMS method [2, 3] in an isothermal reservoir of nitrogen, T = 10,000K.

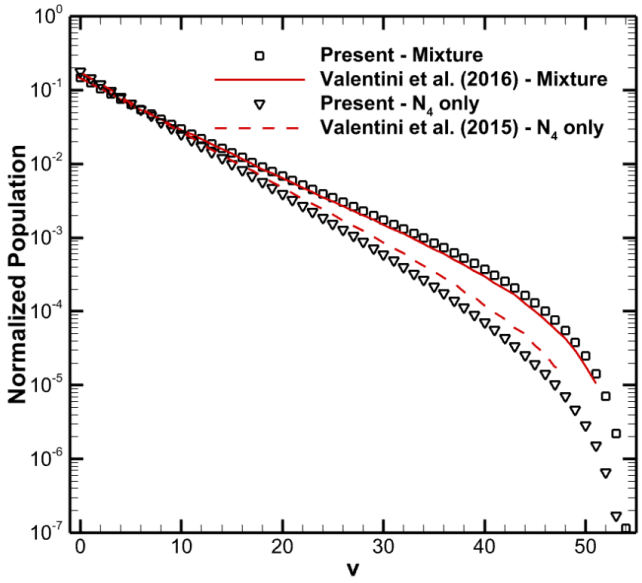

Figure 3.8: Comparison of QSS vibrational distributions between the present vibrational-based grouping model and the DMS method [2, 3] in an isothermal reservoir of nitrogen, T = 20,000K.

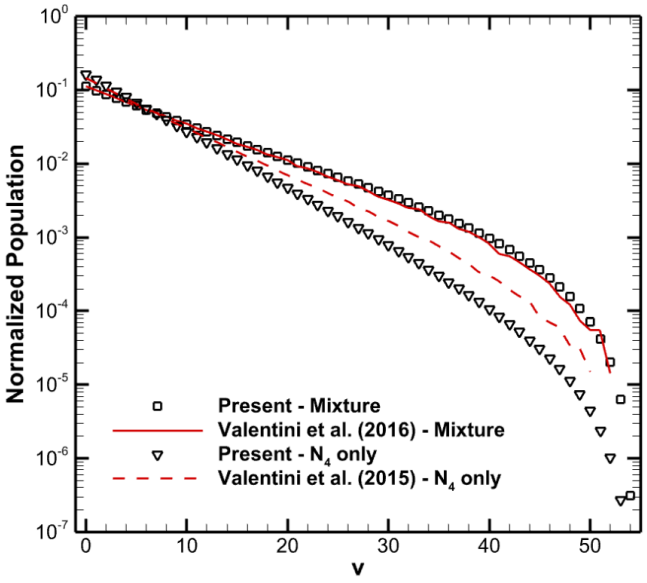

Figure 3.9: Comparison of QSS vibrational distributions between the present vibrational-based grouping model and the DMS method [2, 3] in an isothermal reservoir of nitrogen, T = 30,000K.

The dissociation PDFs corresponding to the QSS distributions shown in Fig.'s 3.7-3.9 are provided in Fig.'s 3.10-3.12. Also shown in these figures are the cumulative density functions (CDFs) for the vibrational-specific model, which provide a metric of the total fraction of dissociated molecules up to a given vibrational state. Because energy transfer in collisions of molecular nitrogen with atomic radicals is an efficient mode of equilibration — due to the enhanced probability of energy scrambling exchange events [3] — dissociation PDFs from the vibrational-specific model mixture cases are similar in shape to the DMS method for all temperatures, whereas vast differences can be seen for the cases which consider only N_2–N_2 interactions. In these N_4 only cases, the dissociation PDFs shift toward the lower end of the vibrational ladder much faster in the vibrational-specific model than the DMS model as the temperature is increased. This stems from the combination of the slower means of vibrational relaxation compared to the mixture case and the vibrational-based grouping strategy assumed. Because the rotational temperature is higher in the vibrational-specific model than the DMS model during dissociation, the weight of highly dissociative upper rotational states (a majority of which are grouped with low vibrational states) on the total dissociation rate is larger in the vibrational-specific model. The increased populations of low vibrational states in the N_4 only cases compared to the mixture cases then allows these rotational states to play a larger role in increasing dissociation. However, once atomic nitrogen is considered, the QSS vibrational temperature is raised, the system moves closer to equilibrium, and molecule-atom collisions quickly repopulate dissociating upper vibrational states. These differences in dissociation PDFs are most apparent in the 30,000K case, shown in Fig. 3.12. Because molecules in the N_4 only case dissociate before having a chance to become excited to the upper vibrational levels, the vibrational distribution tails, denoted by the gradient symbols in Fig.'s 3.7-3.9, are depleted compared to the DMS method predictions, and the dissociation PDFs are shifted to the low-lying vibrational states. This is an important result, as it indicates that resolving only vibrational state kinetics is likely 'good enough' for many hypersonic applications. This conclusion will be tested in the following section through direct comparisons to the DMS method by way of species composition predictions in post-shock conditions.

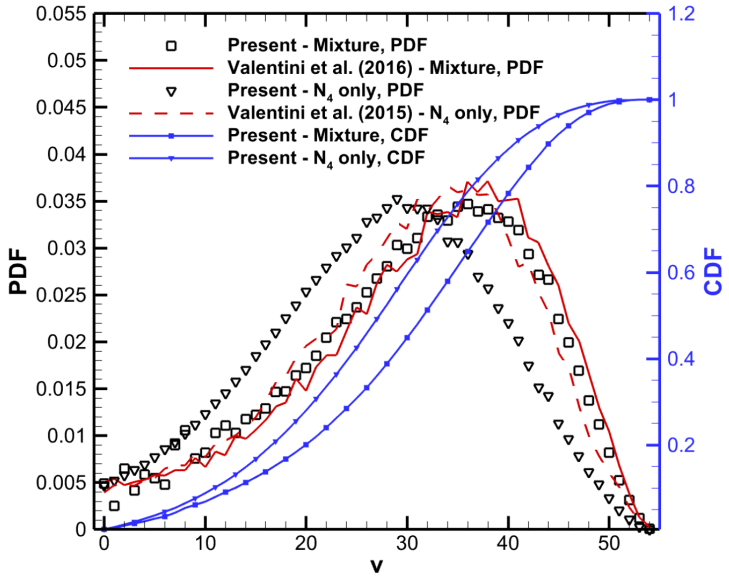

Figure 3.10: Comparison of QSS dissociation probability density functions between the present vibrational-based grouping model and the DMS method [2, 3] in an isothermal reservoir of nitrogen, T = 10,000K.

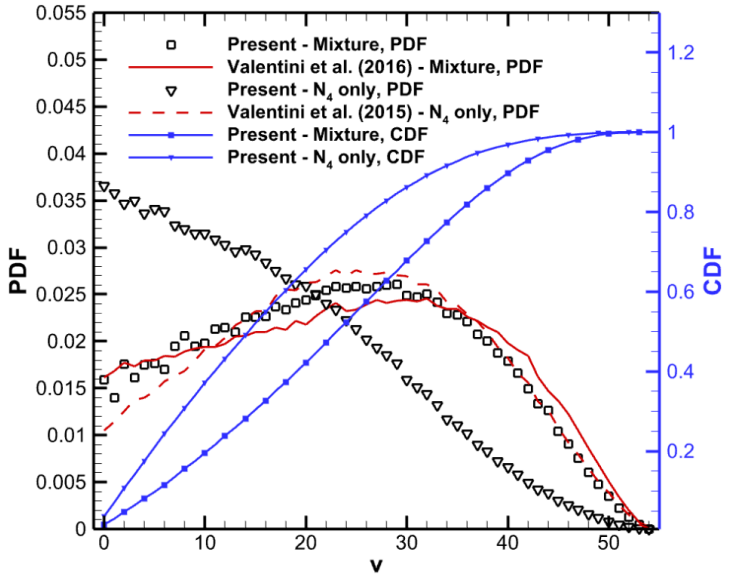

Figure 3.11: Comparison of QSS dissociation probability density functions between the present vibrational-based grouping model and the DMS method [2, 3] in an isothermal reservoir of nitrogen, T = 20,000K.

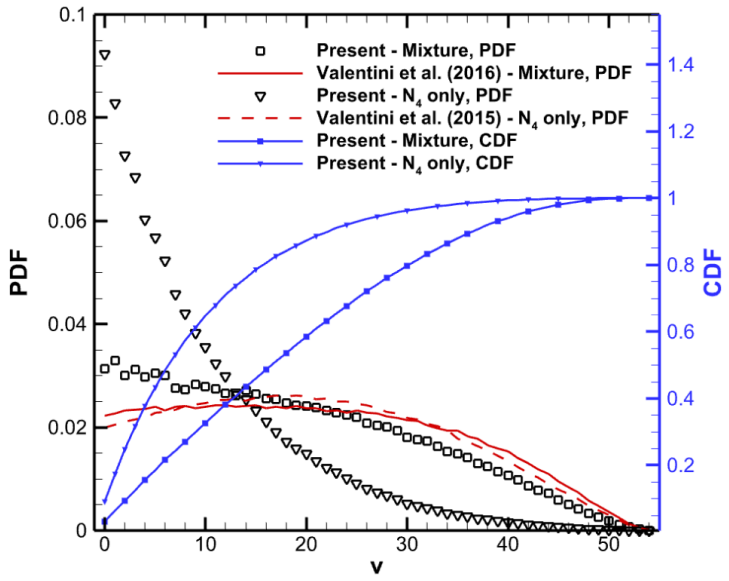

Figure 3.12: Comparison of QSS dissociation probability density functions between the present vibrational-based grouping model and the DMS method [2, 3] in an isothermal reservoir of nitrogen, T = 30,000K.

Very similar characteristics were observed at the microscopic level in the oxygen system. The QSS vibrational distributions and dissociation PDFs for the oxygen mixture and 'O_4 only' cases at 6,000 and 12,000 K are provided in Fig.'s 3.13 and 3.14, respectively, for reference.

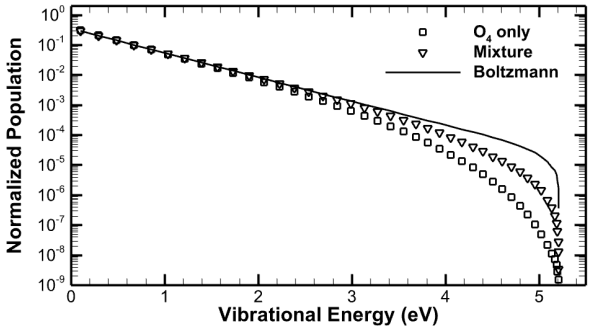

(a) T = 6,000K

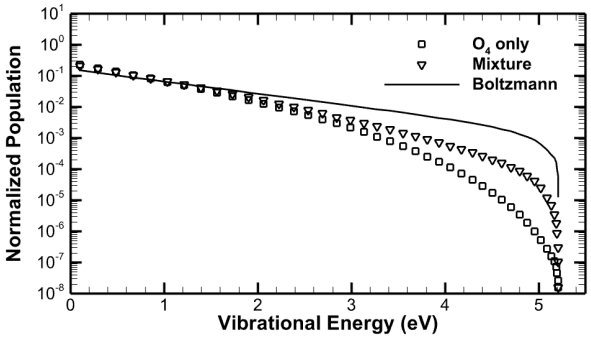

(b) T = 12,000K

Figure 3.13: Oxygen QSS vibrational state distributions.

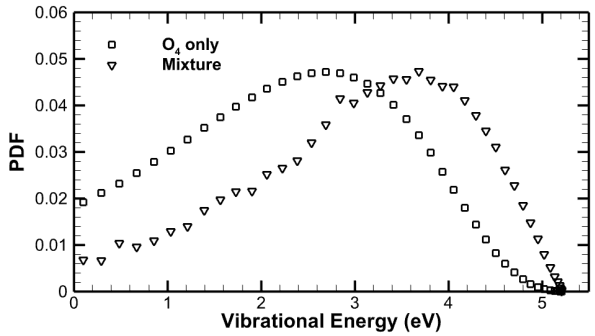

(a) T = 6,000K

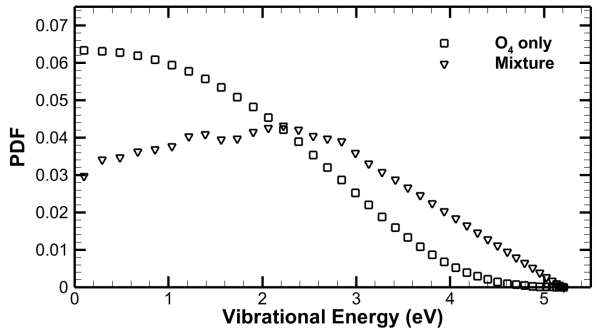

(b) T = 12,000K

Figure 3.14: Oxygen QSS probability density functions.

3.3 Comparison to the DMS method under adiabatic conditions: further assessing the assumption of translational-rotational equilibrium

The following two sections further assess the assumption of translational-rotational equilibrium through comparisons with the DMS method in realistic adiabatic post-shock conditions (as opposed to the idealistic isothermal conditions in the previous section). Both nitrogen and oxygen binary mixtures are examined in detail.

3.3.1 Nitrogen mixtures

Torres and Schwartzentruber [4] conducted a number of 0-D adiabatic reservoir nitrogen mixture calculations using the DMS method. Three of their cases (cases 2-4) are reproduced in this work using the present vibrational-specific model. To avoid confusion, the same case numbering

as Torres and Schwartzentruber is used. Initial conditions for each case are summarized in Table 3.1. To obtain the initial conditions, the total energy and number density are set equal to the corresponding DMS method case (note that a model which assumes translational-rotational equilibrium, such as the present one, begins at a much lower translational temperature than one that does not, such as the DMS model, because the total energy must be consistent between models). The simulations are also run using both the Park and MF models in order to analyze an entire spectrum of fidelity: from the efficient two-temperature models, to the middle ground vibrational model, to the highest-fidelity rovibrational DMS model.

Table 3.1: Initial nonequilibrium conditions for the adiabatic reservoir test cases considered. Initial composition is N_2 only.

Case	**T [K]**	**T_v [K]**	**p [kPa]**
2	36,025	300	31.89
3	24,760	300	19.45
4	14,330	300	8.958

Fig.'s 3.15 and 3.16 show the temperature and atomic nitrogen mole fraction profiles, respectively, for the three cases. To avoid cluttering in Fig. 3.15, only the translational and vibrational temperatures of the present ME model are shown, along with the vibrational temperature data of Torres and Schwartzentruber. Because of the rigid-rotor/harmonic oscillator assumption in the MT models, equilibrium compositions and temperatures are not exactly equal between the models.

At early times, the translational temperatures drop as VT transitions shift energy from the translational to the vibrational mode. For the high-temperature cases (cases 2 and 3), dissociation occurs early on in the excitation process, as there is sufficient energy in the system for molecules to dissociate from a larger portion of the energy ladder.

The agreement between the present vibrationally-resolved ME model and the DMS method

is excellent for cases 3 and 4. Although dissociation is slightly delayed in the present model's case 4 results (because molecules tend to climb to quasi-bound states at lower temperatures before dissociating — a majority of which have been grouped with the low-lying vibrational states in the vibrational-specific model), once nitrogen radicals are introduced into the system, this effect is minimized. Because atomic nitrogen is many times more efficient in transferring energy and causing multi-quantum transitions than molecular nitrogen, good agreement at both macroscopic and microscopic levels (see Fig.'s 3.7-3.12) is observed between models, even though translational-rotational equilibrium is assumed in one of them. This suggests that grouping strategies become less important as more efficient energy transfer channels become available. However, the assumption of translational-rotational equilibrium becomes more apparent in the highest nonequilibrium case studied (case 2), where dissociation occurs noticeably faster than the DMS method.

Although the MF dissociation model is clearly superior to the Park model with a constant vibrational energy loss term, it consistently predicts faster initial dissociation than the ME and DMS models. This is partially because the MF model relies on the Millikan and White relaxation times, which, as shown in Fig. 3.3, result in faster excitation than the QCT data. Since the MF model is based on the idea that collisions are "instantaneous", it provides a much more accurate depiction of the physics at the highest nonequilibrium case than the Park model. At these high temperatures, particle velocities are large enough that the intricate details of the PES, which are captured by the ME and DMS models, become less influential.

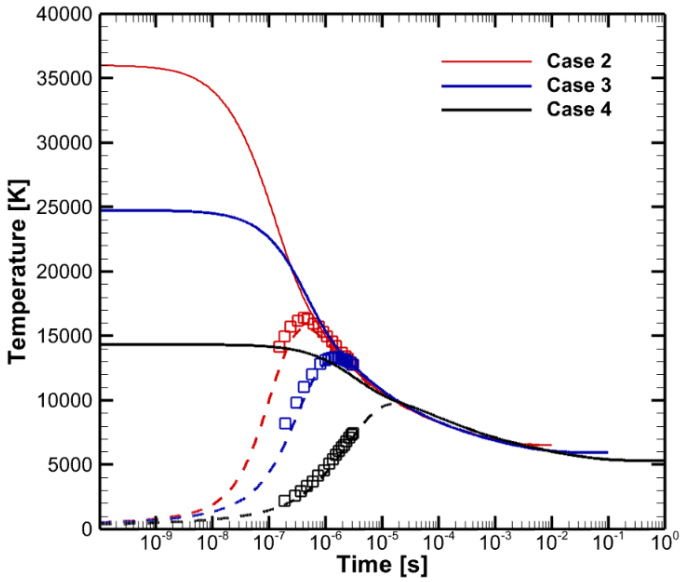

Figure 3.15: Translational and vibrational temperatures in 0-D adiabatic reservoirs. Solid and dashed curves are present model translational and vibrational temperature predictions, respectively. Symbols are DMS vibrational temperature predictions [4].

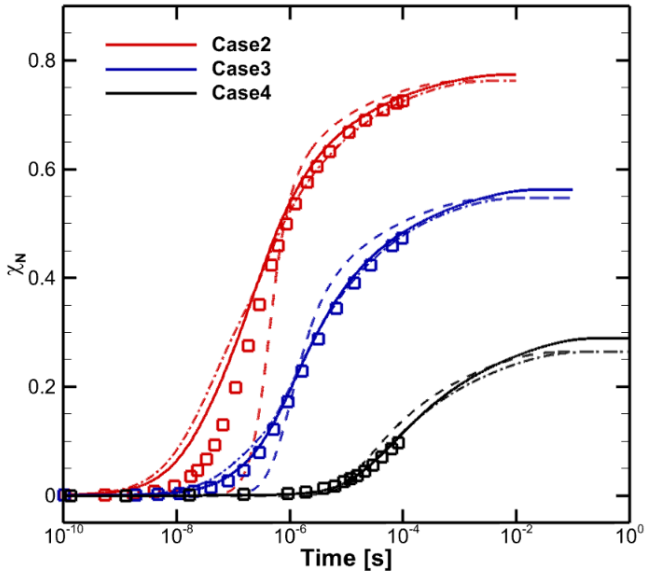

Figure 3.16: Atomic nitrogen mole fraction predictions in 0-D adiabatic reservoirs. Solid curves are the present model, symbols are DMS [4], dashed curves are Park's model, and dash-dotted curves are the MF model.

Fig. 3.17 shows a zoomed image of the initial dissociation regions for each case. The inadequacies of the Park model in accurately capturing dissociation in high thermal nonequilibrium environments becomes clear, as dissociation is significantly delayed when compared to the other models.

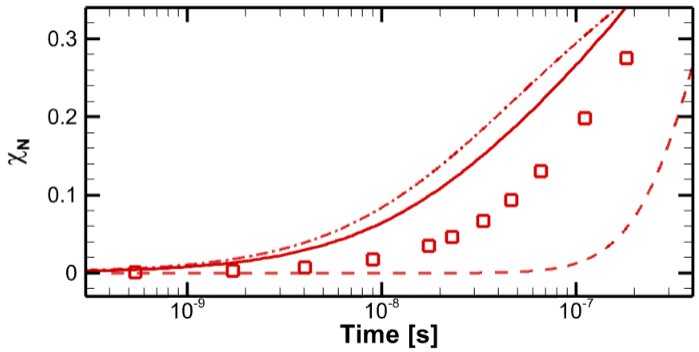

(a) Case 2

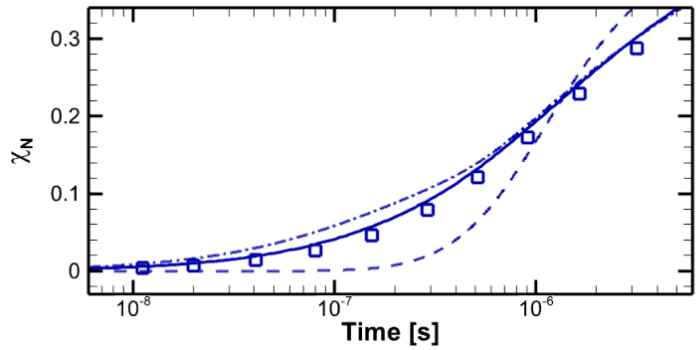

(b) Case 3

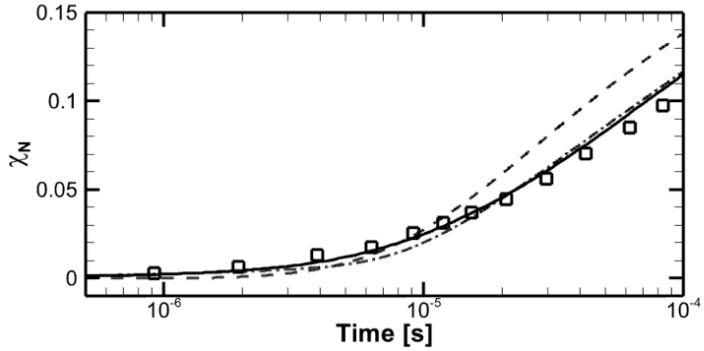

(c) Case 4

Figure 3.17: Initial dissociation regions in adiabatic reservoir test cases. Line styles correspond to those in Fig. 3.16.

To further study how dissociation is occurring in these simulations, three separate dissociation rate coefficients are extracted from the vibrational-specific model's results: 1) an instantaneous

dissociation rate coefficient based on instantaneous vibrational state populations, K_d^{inst}, 2) an instantaneous nonequilibrium dissociation rate coefficient based on a Boltzmann distribution of vibrational states at the instantaneous vibrational temperature, $K_d^{neq}(T, T_v)$, and 3) an instantaneous equilibrium dissociation rate coefficient based on a Boltzmann distribution of vibrational states at the instantaneous translational-rotational temperature, $K_d^{eq}(T)$. Dissociation due to atomic and molecular collisions are analyzed separately using the dissociation rate coefficient expression

$$K_d = \frac{\sum_v D_v^{sys} n_v}{n_{N_2}} \tag{3.1}$$

where the superscript sys designates either N_2–N or N_2–N_2, and only the vibrational populations vary between K_d^{inst}, $K_d^{neq}(T, T_v)$, and $K_d^{eq}(T)$. These instantaneous dissociation rate coefficients are compared in Fig. 3.18 for both atom (a) and molecule (b) collision partners for case 4. Also plotted are the z-factors, defined as the ratio of K_d^{inst} to $K_d^{eq}(T)$ — i.e. the z-factor equals 1 when equilibrium dissociation occurs. The vertical lines symbolize the temporal locations at which 10% and 90% of the equilibrium atomic mole fraction is reached.

Similar characteristics are observed for molecule-molecule and molecule-atom dissociation. Initially, K_d^{inst} is much lower than the thermal equilibrium rate and is identical to the equilibrium rate with a Boltzmann distribution at T_v. However, as the solution progresses, K_d^{inst} first rises above $K_d^{neq}(T, T_v)$, then dips and stays below the other rates until final equilibration. The initial rise above $K_d^{neq}(T, T_v)$ is a result of the initial overpopulation of upper vibrational energy levels at early times due to efficient energy transfer between these closely spaced levels, which are being preferentially dissociated. However, a depleted vibrational energy tail soon forms and, consequently, K_d^{inst} drops below the other two rates.

One important feature to note from these profiles is that a large portion of the dissociation occurs after the vibrational and translational temperatures, and hence $K_d^{neq}(T, T_v)$ and $K_d^{eq}(T)$, are nearly equilibrated. This may lead to inaccuracies in two-temperature models, which rely solely on T and T_v information. Clearly, K_d^{inst} is still far below the equilibrium dissociation rate coefficients after this near-equilibration.

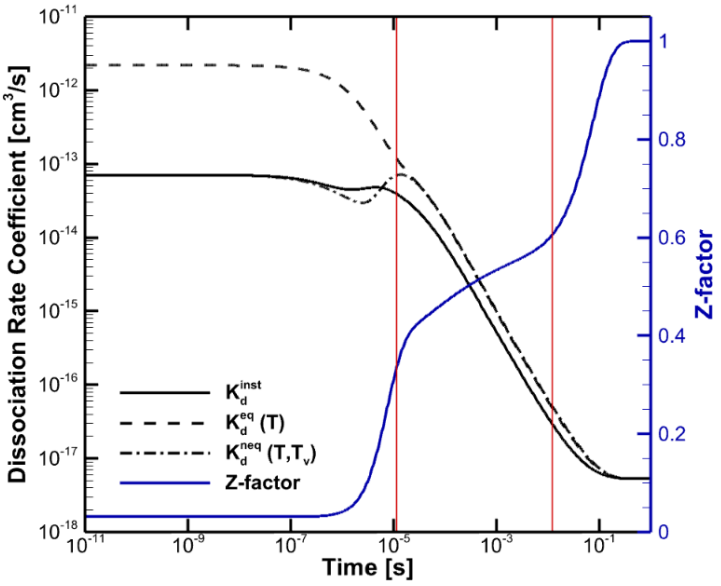

(a) N_2–N

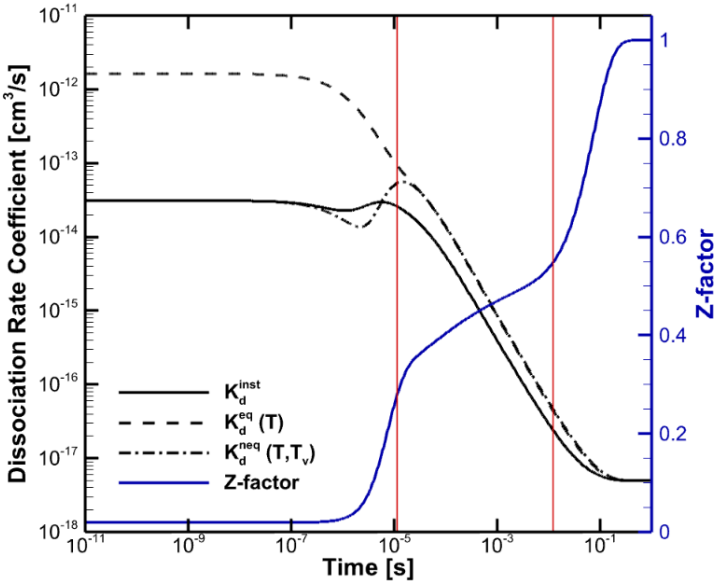

(b) N_2–N_2

Figure 3.18: Instantaneous dissociation rate coefficients and z-factors in the adiabatic reservoir case 4. Vertical red lines symbolize temporal locations at which 10% and 90% of the equilibrium atomic mole fraction is reached.

Additionally, as pointed out by Torres and Schwartzentruber [79], dissociation in adiabatic reservoirs occurs through transient QSS-like phases. Even though the temperatures are nearly

equilibrated, dissociation is suppressed due to a depletion of the vibrational energy distribution tail. To verify this assertion, vibrational distributions are extracted from the adiabatic simulations at the point at which the translational temperature is (approximately) equal to 10,000K. Table 3.2 lists the points at which the vibrational distributions are extracted from the adiabatic simulations.

Table 3.2: Conditions at which vibrational distributions are extracted from adiabatic simulations and compared in Fig. 3.19.

Case	**t [s]**	**T [K]**	**T_v [K]**
2	1.6264e-5	9,999	9,970
3	1.8604e-5	10,000	9,984
4	1.6504e-5	10,001	9,738

Similar to Torres and Schwartzentruber, these distributions are then compared to the distribution obtained during the QSS phase of an isothermal heat bath at 10,000K. The results are shown in Fig. 3.19. The isothermal QSS and adiabatic populations are remarkably similar. The vibrational temperature corresponding to case 4's distribution is lower than the other cases — see Table 3.2 — and its vibrational energy tail is less depleted because the level of atomic nitrogen (which tends to dominate the collisional dynamics and move the system closer toward equilibrium due to its efficient energy transfer in molecular collisions) at this point is minimal compared to the other cases ($\chi_N = 0.04$). This comparison illustrates that QSS dissociation characteristics extracted from idealistic 0-D isothermal calculations are also applicable to adiabatic post-shock systems.

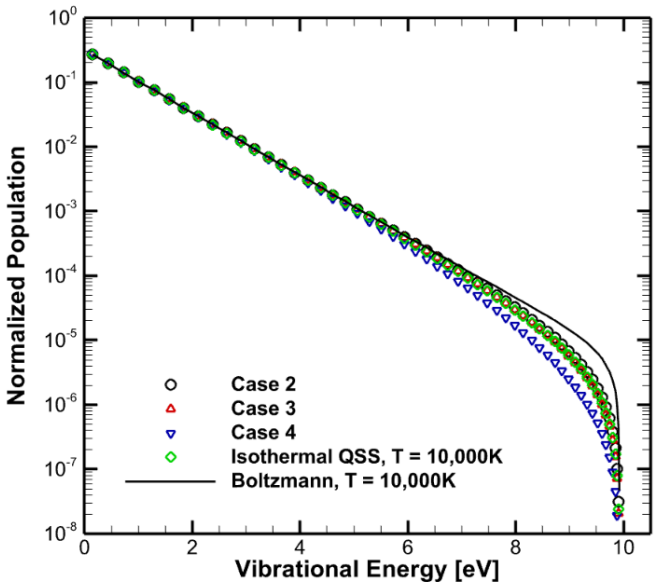

Figure 3.19: Comparison of T = 10,000K isothermal QSS vibrational distribution with adiabatic vibrational distributions when T $\approx$ 10,000K.

To further study rovibrational coupling in normal shock flows of nitrogen, Schwartzentruber et al. [5] conducted a number of 1-D DMS method calculations using simplified potentials (Ling-Rigby and Taylor-6 oscillator for intermolecular and intramolecular forces, respectively). Dissociation was not modeled in these simulations. Each case from [5] is reproduced here using the vibrational-specific model. A comparison of the temperature profiles is shown in Fig. 3.20. Also shown are results from the present model when dissociation is considered. Because the present ME model does not resolve the shock structure (the Rankine-Hugoniot relations are used to obtain initial post-shock conditions), the initial post-shock location in the present model is aligned with the location of the peak translational temperature in the DMS calculations. For all cases, the freestream atmospheric conditions correspond to 40km of altitude, and only the freestream velocity, u_0, is varied.

Despite Schwartzentruber et al. using simplified potentials, the agreement with the present model is good for all cases. Additionally, when dissociation is considered, the initial excitation phase is mostly unaffected, indicating the presence of the incubation period. Although direct com-

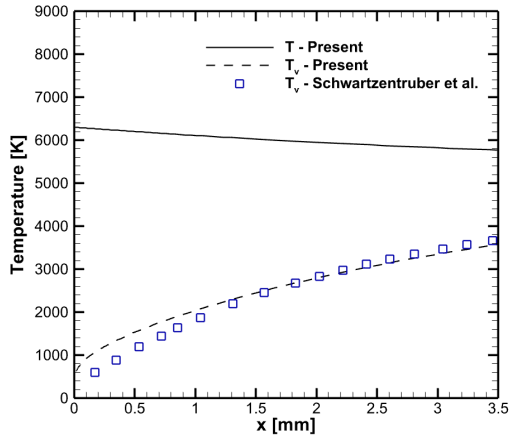

(a) $u_0 = 3,599.6$ m/s

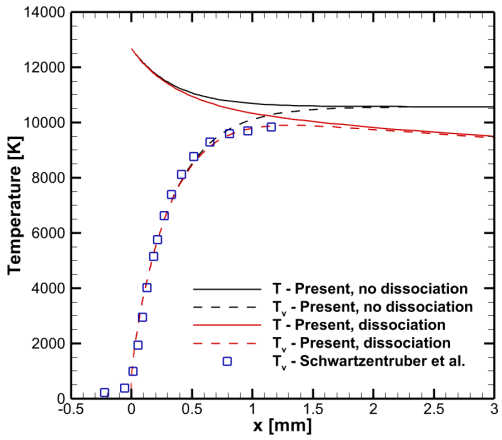

(b) $u_0 = 5154.4$ m/s

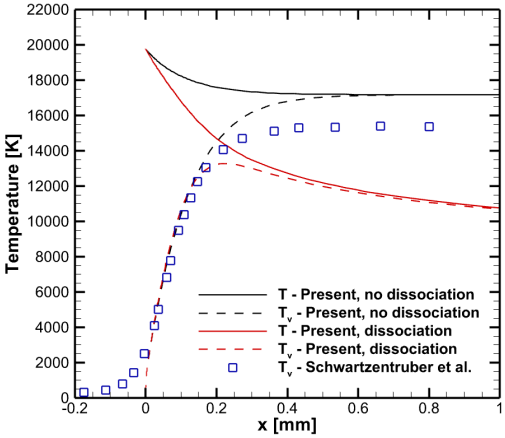

(c) $u_0 = 6,459.6$ m/s

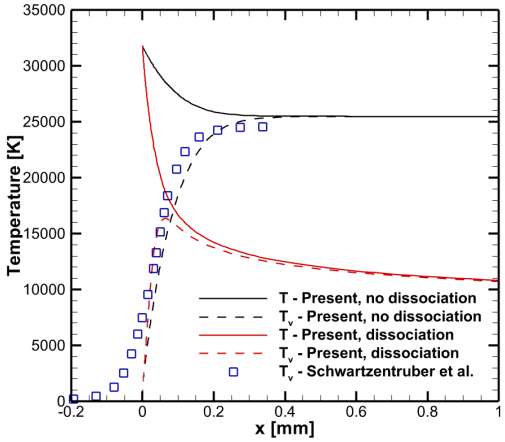

(d) $u_0 = 8,206.9$ m/s

Figure 3.20: Comparison of 1-D post-shock temperature profiles. Dissociation is not considered in Schwartzentruber et al.'s [5] DMS calculations.

parisons to 1-D DMS method calculations with dissociation considered would provide additional insight, these (and the adiabatic) comparisons still show an important point in that nonequilibrium thermochemistry effects associated with rotational degrees of freedom have a minor effect on the relaxation of the vibrational mode for a wide range of hypersonic conditions.

3.3.2 Oxygen mixtures

To further affirm the physics observed in the previous section, additional comparisons to the DMS method using the present oxygen kinetic database are provided in this section.

Torres and Schwartzentruber [6] studied the pure oxygen shock-tube experiments of Ibraguimova et al. [8] using the DMS method by first creating equivalent 0-D adiabatic reservoirs. This allowed for a direct assessment of the applicability and physicality of the simplified 0-D simulations. It was shown that excitation and dissociation are much more gradual in the 1-D case, as the bulk kinetic motion slowly 'pumps' energy into the internal modes of the molecules.

The three 0-D adiabatic oxygen reservoir cases of Torres and Schwartzentruber are reproduced using the present model for comparison. Again, the DMS method does not decouple internal modes, thus these comparisons provide insight into the influence of rotational nonequilibrium. To conform with the DMS method calculations, the non-adiabatic correction factor, $\eta = 16/3$, is not applied to either O_2–O or O_2–O_2 dissociation. Ibraguimova et al. conducted a number of shock-tube runs; however, three cases are chosen for their various degrees of nonequilibrium. The initial conditions for each adiabatic reservoir case are listed in Table 3.3, where LNEQ, MNEQ, and HNEQ stand for low, medium, and high nonequilibrium, respectively.

Table 3.3: Initial nonequilibrium conditions for the 0-D adiabatic reservoir cases. Initial composition is O_2 only.

Case	**T (K)**	**T_v (K)**	**p (kPa)**
LNEQ	6,181	298.2	55.34
MNEQ	10,502	298.2	62.83
HNEQ	13,340	298.2	71.22

Fig. 3.21 shows the vibrational-specific model's atomic oxygen mole fraction predictions (solid and dashed curves) for each case compared to the results of the DMS method calculations (square symbols). The corresponding temperature profiles are shown in Fig. 3.22. The translational temperatures from Torres and Schwartzentruber are not shown for readability.

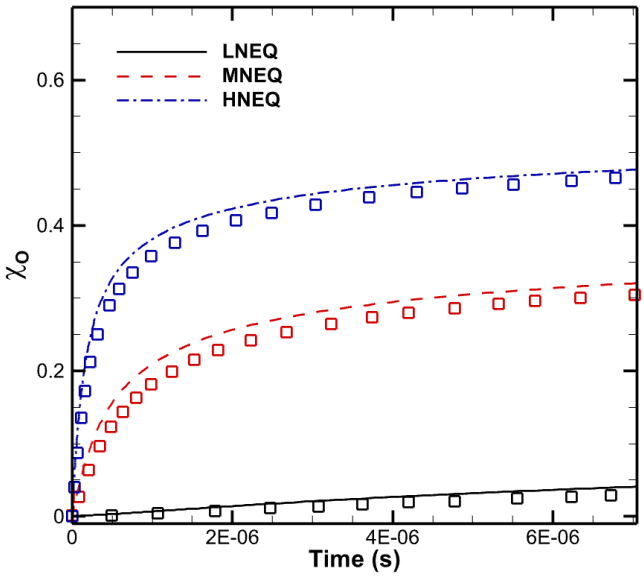

Figure 3.21: Atomic oxygen mole fraction profiles in 0-D adiabatic reservoirs. Curves designate present calculations, and symbols designate the DMS method results of Torres and Schwartzentruber [6].

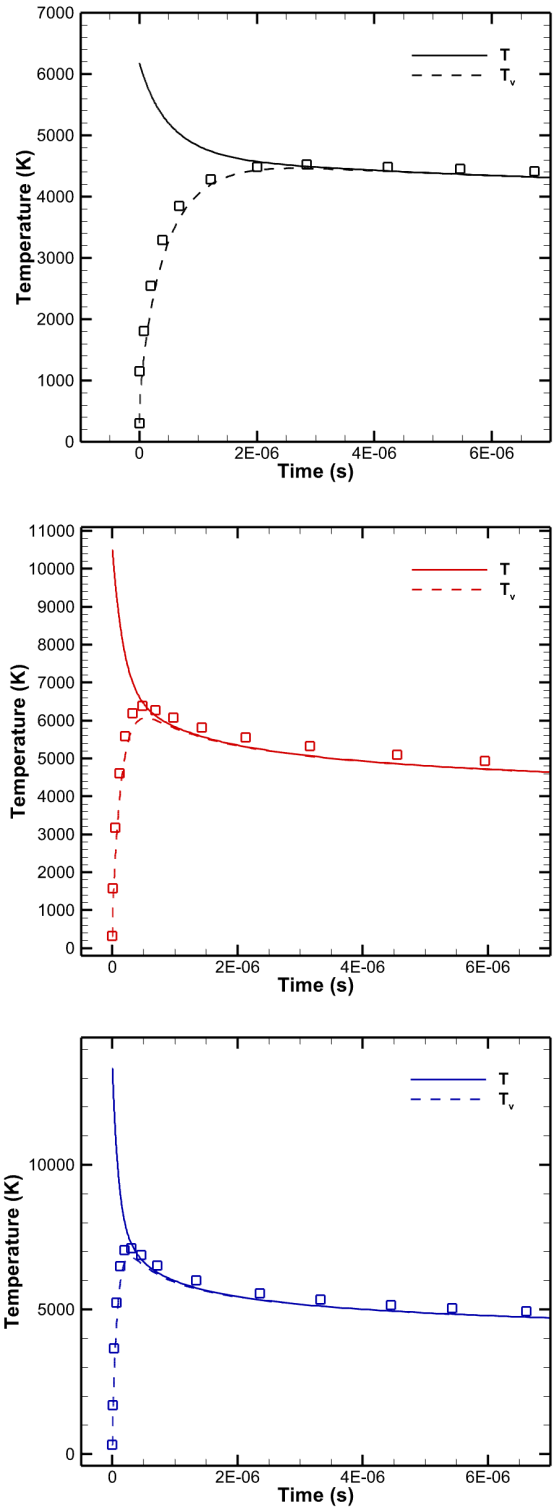

Figure 3.22: Translational and vibrational temperature profiles in 0-D adiabatic reservoirs. Curves designate the present results, and the DMS method vibrational temperatures [6] are designated by square symbols (LNEQ, MNEQ and HNEQ from top to bottom).

The vibrational-specific model predicts slightly faster dissociation for all cases; however, the magnitude of dissociation is very similar between models. The increased level of dissociation in the present model can be attributed to two mechanisms: 1) employing only the triplet O_4 PES (the DMS calculations consider all three PESs corresponding to ground-state collisions of two oxygen molecules), and 2) the assumption of translational-rotational equilibrium. The former point is supported by Chaudhry et al.'s QCT analysis of the O_4 system [42], which shows that the triplet surface is more dissociative than either the singlet or quintet surfaces. Grover et al. [48] show that vibrational excitation is somewhat slower on the triplet surface than the full O_4 system. This results in a small trade-off with the faster dissociation. It is expected that better agreement with the DMS method would result if the full O_4 system were implemented in the present model.

Although already hinted at in the previous section, an additional discussion should be given to the second reason attributed to the faster dissociation observed by the present model: the assumption of translational-rotational equilibrium. Macdonald et al. [80] pointed out that dissociation in the N_2–N_2 collisional system is delayed at low temperatures in models that group based on vibrational quantum numbers, due to the fact that quasi-bound states are grouped together with bound states. At lower temperatures, molecules tend to climb to these quasi-bound states before dissociating. This causes a suppression in dissociation, even though the assumption of translational-rotational equilibrium implies quasi-bound states are overpopulated. At higher temperatures, however, the assumption of translational-rotational equilibrium plays a larger role, as molecules begin dissociating from a larger portion of the vibrational ladder. This leads to the opposite effect: dissociation occurs faster in the vibrational-based grouping model when compared to a rovibrational model. Although this phenomenon also likely occurs in O_2–O_2 dissociation, one key detail to note is that grouping strategies become less important as energy transfer channels become more efficient. In the case of oxygen, once atomic oxygen radicals are present in the flow, the importance of the grouping strategy on dissociation becomes lessened, as atomic oxygen is very efficient at transferring energy in collision events. Because of this, just as in the nitrogen case comparisons in the previous section, the influence of rotational nonequilibrium appears to be minimal and the

agreement with the DMS method is good. These results are encouraging because the vibrational-specific model comes at a fraction of the cost. A typical 0-D adiabatic case takes approximately 2 core-min. to complete.

3.4 Numerical modeling of shock-tube experiments

The following three subsections examine the pure oxygen shock-tube experiments of Streicher et al. [7] and Ibraguimova et al. [8] and the pure nitrogen shock-tube experiment of Sharma and Gillespie [10] via the numerical modeling techniques described in Sections 2.3.3 and 2.3.4.

3.4.1 Streicher et al. (2021)

Streicher et al. report time-histories of vibrational temperature and composition for three pure oxygen cases. These three experimental runs are modeled here using three approaches 1) Park's two-temperature model under the assumptions of a frozen vibrational mode and frozen chemistry for determining the initial region 5 conditions (as is done by Streicher et al.), which will be denoted 'FF: 2T Park' in the figures, 2) the QCT-ME model under the assumptions of a frozen vibrational mode and frozen chemistry for determining the initial region 5 conditions, which will be denoted 'FF: QCT-ME', and 3) the QCT-ME model which considers relaxation behind both the incident and reflected shocks — as detailed in Section 2.3.4 — which will be denoted 'NN: QCT-ME' in the figures and abbreviated simply as 'NN' in the text. The initial fill pressure and incident shock velocity conditions for each case are detailed in Table 3.4, where the same case numbering as Streicher et al. is used.

Table 3.4: Initial conditions for the reflected shock relaxation cases considered.

Case	p_{fill} **(Torr)**	u_{is} **(km/s)**
100-1	0.13	2.22
100-6	0.07	2.51
100-8	0.05	2.76

Because the NN model accounts for relaxation in region 2, it provides a direct mechanism for assessing the frozen chemistry and frozen vibrational mode assumptions commonly made when modeling reflected shock relaxation. Figures 3.23 and 3.24 show the post-incident shock temperature and atomic oxygen mole fraction profiles, respectively, for each case in Table 3.4. The termination of the profiles signifies the particle time required to reach and become stagnated at the measurement location by the arrival of the reflected shock, t_e. The degree of dissociation in Fig. 3.24 remains much less than 1% for all cases, implying that the frozen chemistry assumption is an appropriate simplification. However, the temperature profiles in Fig. 3.23 suggest that assuming a frozen vibrational mode may lead to erroneous predictions for the initial region 5 vibrational and translational temperatures. Hanquist et al. [61] discuss similar findings regarding the degree of vibrational excitation behind the incident shock. Unlike Hanquist et al., however, the post-incident shock vibrational excitation is accompanied by a non-negligible drop in the translational temperature in the present calculations. Because Hanquist et al. modeled oxygen mixtures that were heavily diluted by argon, the gas temperatures in their simulations were nearly constant in region 2. This is not the case when pure oxygen is used as the test gas, as more translational energy is required to excite the vibrational mode in pure O_2 mixtures.

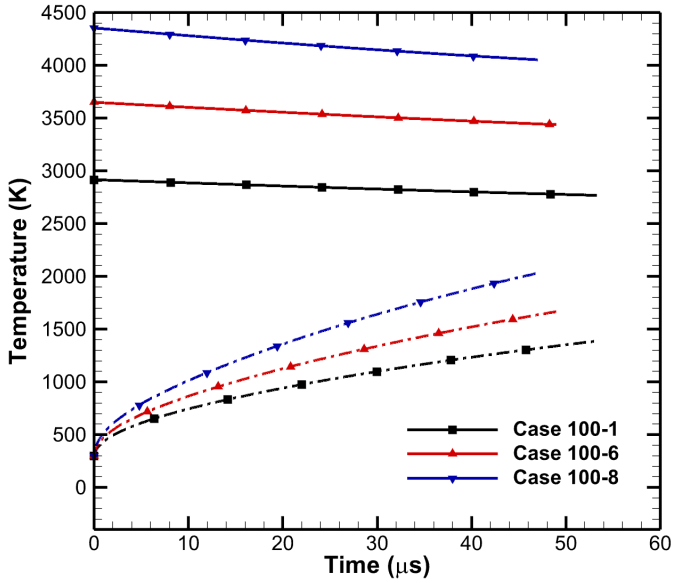

Figure 3.23: Translational temperature (solid profiles) and vibrational temperature (dash dot profiles) predictions behind the incident shock waves of Streicher et al.'s [7] shock-tube experiment.

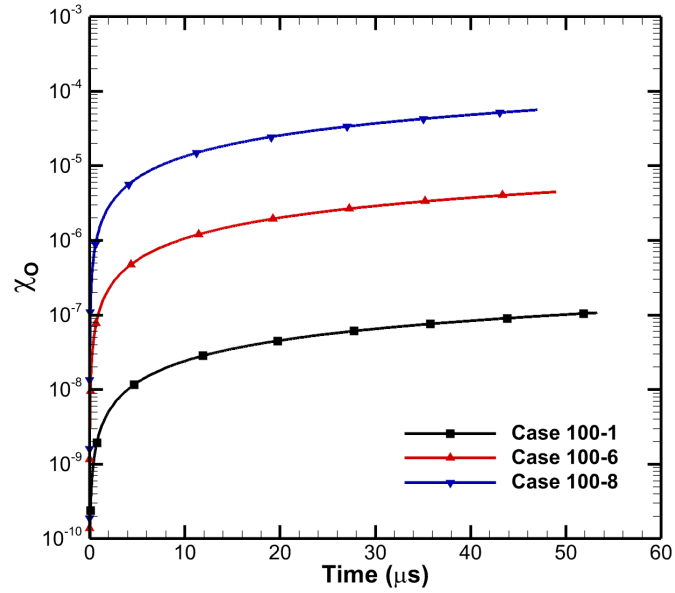

Figure 3.24: Atomic oxygen mole fraction predictions behind the incident shock waves of Streicher et al.'s [7] shock-tube experiment.

Table 3.5 elucidates the differences in initial region 5 thermodynamic quantities obtained under the FF (frozen vibrational mode through both shocks) and NN (nonequilibrium relaxation accounted for in region 2) assumptions. Also tabulated are the results of Streicher et al. for all 8 pure oxygen cases reported. Streicher et al. use the FF assumption to obtain the initial region 5 translational and vibrational temperatures; however, the pressure was directly measured. The values in parentheses designate how much larger or smaller, by percent, the quantity is than Streicher et al.'s experimental pressure measurement or FF-computed temperature. Because it is not reported, the initial region 1 temperature is assumed to be 300 K for every case.

Table 3.5: Initial post-reflected shock conditions. Quantities in parentheses indicate percent larger or smaller than Streicher et al.'s [7] tabulated conditions.

Model	**Case**	T^0 **(K)**	T_v^0 **(K)**	p^0 **(Torr)**
Streicher et al. (exp.)	100-1	6230	300	57
	100-2	6300	300	89
	100-3	6800	300	63
	100-4	6890	300	37
	100-5	7340	300	30
	100-6	7940	300	41
	100-7	8750	300	26
	100-8	9560	300	34
FF	100-1	6230	300	48.9 (-14.2)
	100-2	6300	300	72.2 (-18.9)
	100-3	6800	300	53.9 (-14.4)
	100-4	6890	300	33.8 (-8.6)
	100-5	7340	300	22.5 (-25.0)
	100-6	7940	300	34.5 (-15.8)
	100-7	8750	300	22.0 (-15.4)
	100-8	9560	300	30.2 (-11.2)
NN	100-1	5934 (-4.8)	1388	56.4 (-1.1)
	100-2	5910 (-6.2)	1665	86.7 (-2.6)
	100-3	6389 (-6.0)	1659	64.3 (+2.1)
	100-4	6593 (-4.3)	1368	38.5 (+4.1)
	100-5	7046 (-4.0)	1223	25.0 (-16.7)
	100-6	7449 (-6.2)	1666	40.8 (-0.5)
	100-7	8286 (-5.3)	1549	25.4 (-2.3)
	100-8	8814 (-7.8)	2031	37.5 (+10.3)

If vibrational relaxation in region 2 is not accounted for, i.e. the FF assumption is used, the initial region 5 pressure is underestimated by 8-25% when compared to the experiment. However, when the NN model is employed along with the present set of QCT rate coefficients, the predicted p^0 is within 5% for all cases except 100-5 and 100-8. Another important characteristic to note from Table 3.5 is the difference in initial region 5 temperatures between the FF and NN models. The NN model predicts vibrational temperatures of around 1500 K by the time the flow is shocked again. Due to the endothermic VT transitions occurring in region 2 and the weakening reflected shock front, the initial region 5 translational temperatures predicted by the NN model are also 4-8% lower than the FF model's predictions. Obtaining physically-consistent initial test conditions is crucial for model validation, thus it is recommended that vibrational relaxation be accounted for in region 2 when numerically simulating or post-processing experimental data from non-diluted reflected shock experiments.

As described by Johannesen et al. [81] and Presley and Hanson [82], endothermic relaxation and dissociation in region 5 lead to an increase in mass density and a subsequent decrease in the reflected shock's strength. Fig. 3.25 shows the reflected shock velocity as a function of distance from the end wall for each case outlined in Table 3.4 using the NN model. The initial velocity at the wall corresponds to the frozen flow velocity, which can be computed from the incident shock Mach number (see Section 7.3 of Anderson [62]). The NN model predicts that u_{rs} drops by approximately 15-20% by the time it reaches the observation location 5mm from the end wall, with faster deceleration occurring in the highest enthalpy case due to the increased level of vibrational excitation and dissociation. Aside from modifying the initial region 5 conditions, the non-constant u_{rs} may lead to additional uncertainties (albeit small) in the post-processing of experimental data, such as in the density correction applied by Streicher et al.

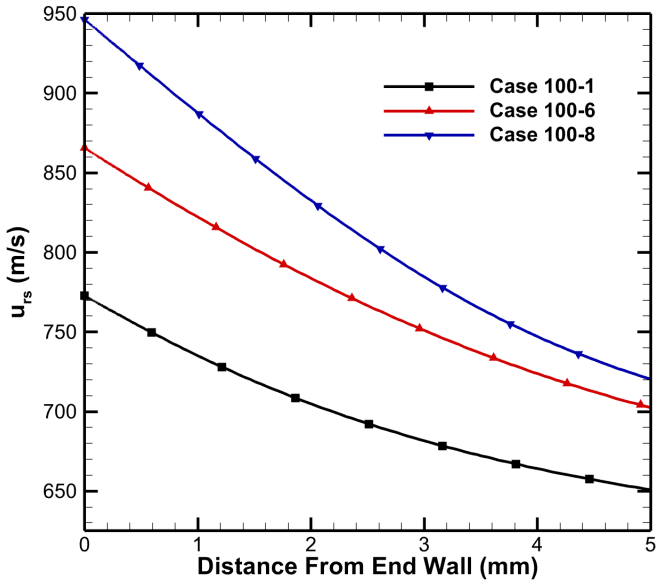

Figure 3.25: Reflected shock velocity as a function of distance from the end wall.

The influence of accounting for the varying u_{rs} on determining the initial upstream conditions for the Rankine-Hugoniot relations at the measurement location is visualized in Fig.'s 3.26 and 3.27. Fig. 3.26 is an x-t diagram of the incident shocks, reflected shocks, and region 2 velocities (i.e. particle paths), and Fig. 3.27 is a zoomed image of the x-t diagram at the near-wall region. The solid reflected shock profiles in Fig. 3.27 correspond to the velocities shown in Fig. 3.25, and the dashed profiles correspond to assuming constant reflected shock velocities. Because u_{rs} decreases with distance from the wall when relaxation is considered, more time is required to reach the measurement location than when a constant u_{rs} is assumed. Table 3.6 summarizes the elapsed particle time, t_e, for each of the three simulated cases using the NN model and assuming constant region 2 and reflected shock velocities. The latter of which can be calculated from the equation derived in Hanquist et al.'s study [61]:

$$t_e = \frac{d(u_{is} + u_{rs})}{u_{rs}(u_{is} - u_2)} \tag{3.2}$$

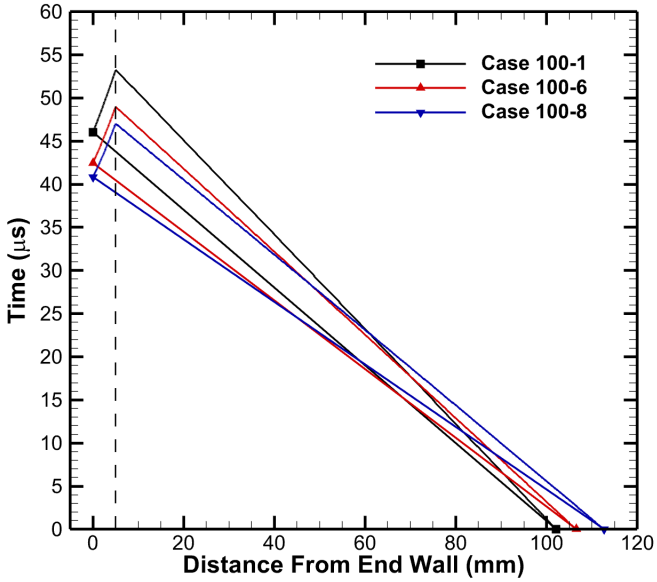

Figure 3.26: x-t diagram of incident shocks, reflected shocks, and region 2 velocities (i.e. particle paths). The black dashed vertical line denotes the observation location.

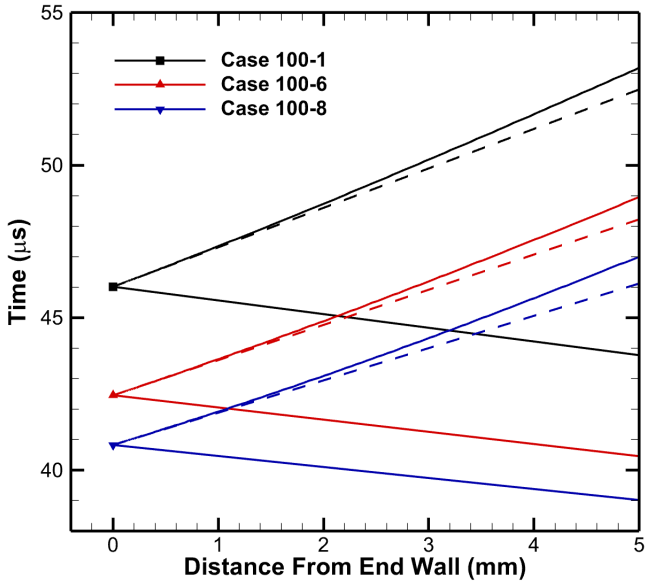

Figure 3.27: x-t diagram of the near-wall region. Dashed reflected shock profiles correspond to a constant u_{rs}, and solid reflected shock profiles correspond to the velocities shown in Fig. 3.25.

Table 3.6: Particle time after passage of incident shock before being stagnated at the observation location, $t_e(\mu s)$.

Case	Const u_2 and u_{rs}	NN
100-1	47.1	53.3
100-6	42.9	49.0
100-8	39.7	47.0

Finally, the time-histories of the region 5 translational and vibrational temperatures for the cases outlined in Table 3.4 are compared in Fig.'s 3.28-3.30. Similar to the 1-D incident shock cases, Park's two-temperature model predicts a much faster peak in vibrational temperature than the other models, and its subsequent drop in translational temperature is more aggressive, as endothermic dissociation occurs more quickly than the other models. Park's two-temperature model under the FF assumption does not fall within any of the reported experimental error bounds for vibrational temperature. The QCT-ME model under the NN assumption leads to vibrational temperature predictions that fall close to or within most of the vibrational temperature error bounds aside from the earliest one in Fig. 3.28, which may be a consequence of Streicher et al. making the frozen vibrational mode assumption when determining the final time-histories reported. The temperatures predicted by the QCT-ME models near the end of the simulations ($50\mu s$) tend to overestimate the data reported in the experiment, with larger differences occurring in the lower temperature cases. As discussed in Section 2.3.4, this may be a result of the numerical model's inability to account for relaxation in region 2 after the initial conditions for the Rankine-Hugoniot relations at the measurement location are obtained. This region 2 relaxation serves to accelerate the shock, albeit on a much larger time scale than that of region 5. Less time would pass if u_{rs} is increased (recall that time is obtained through the relation $dt = dx/u_{rs}$), which would result in faster equilibration of the system, such as that observed by the experiment.

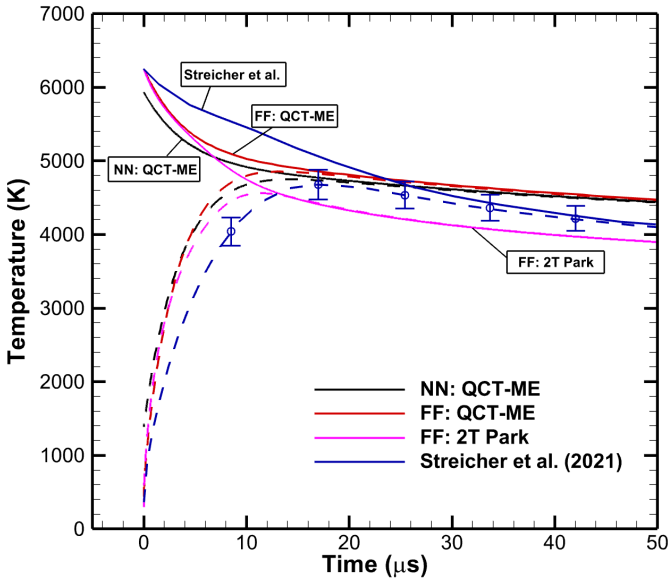

Figure 3.28: Translational temperature (solid profiles) and vibrational temperature (dashed profiles) time-histories, Streicher et al.'s [7] reflected shock case 100-1.

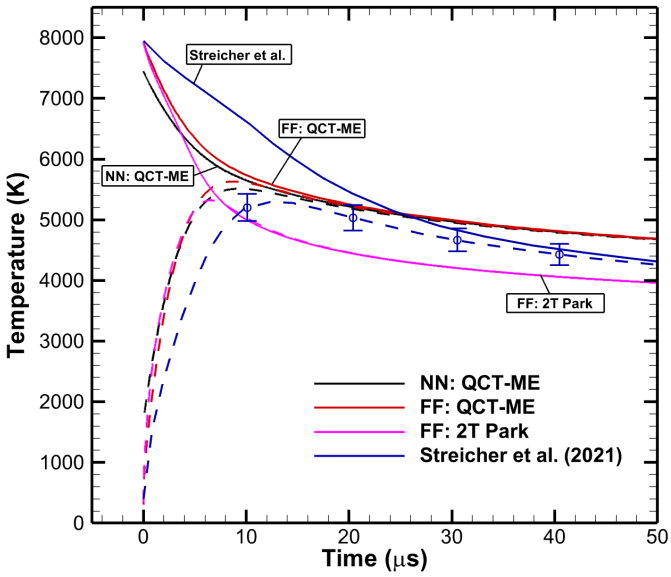

Figure 3.29: Translational temperature (solid profiles) and vibrational temperature (dashed profiles) time-histories, Streicher et al.'s [7] reflected shock case 100-6.

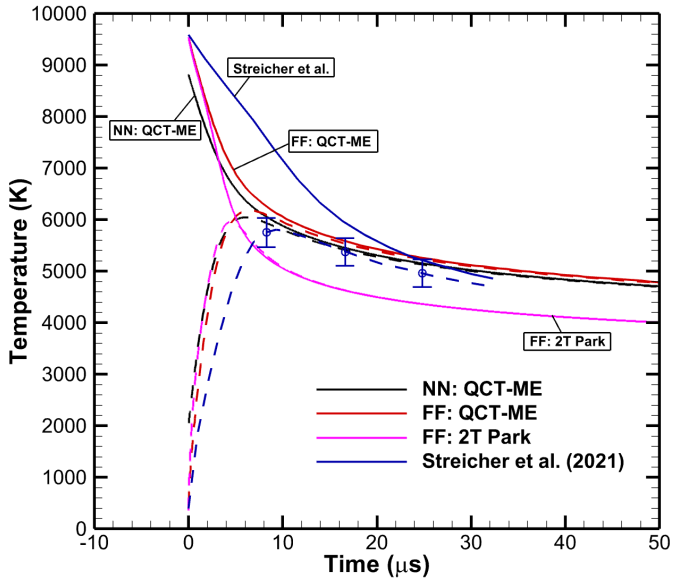

Figure 3.30: Translational temperature (solid profiles) and vibrational temperature (dashed profiles) time-histories, Streicher et al.'s [7] reflected shock case 100-8.

A noticeable difference is observed in the translational temperature behavior between all three computational models and the results reported by Streicher et al. Streicher et al. determined the translational temperature by invoking the conservation of energy equation $dh = vdp$ at the measurement location, where dp is the non-ideal pressure increase measured in the experiment. They then used the NASA Glenn polynomials and knowledge of vibrational temperature and molecular oxygen composition (from diagnostic measurements) to determine the gas temperature. Aside from the base difference in solving separate governing equations, there are two primary reasons why the difference in translational temperature behavior between the models and experiment could occur: 1) the calculation of vibrational energy from vibrational temperature, and 2) the temperature increases due to the non-ideal pressure increases [64], which are not accounted for in the present model.

Additional explanation should be given to the first point: the calculation of vibrational energy from vibrational temperature. Because Streicher et al. first subtracts the vibrational energy at T away from the enthalpy computed at T before adding the vibrational energy at T_v, an overestima-

tion of translational temperature would occur at early times if a simple model, such as the harmonic oscillator model, is used to compute the vibrational energy. This is because the harmonic oscillator model accurately reproduces the vibrational energy of the present O_2 ladder at low vibrational temperatures (i.e. at early times in the simulations); however, the harmonic oscillator model underpredicts the amount of vibrational energy of the present O_2 ladder as temperature is increased. This would imply that not enough energy would be removed for the vibrational energy at T, but the correct amount would be added at T_v at early times, leading to an overprediction of translational temperature.

Nevertheless, the improved predictive capability of the present QCT-ME models over Park's two-temperature model is encouraging. Care should be taken, however, when modeling and post-processing data from reflected shock-tube experiments, as inaccurately determining initial conditions can lead to additional uncertainties that are propagated throughout simulations, making model validation with the experiment difficult.

3.4.2 Ibraguimova et al. (2013)

In the early 2010s, Ibraguimova et al. [8] conducted a set of shock-tube experiments using pure oxygen as the test gas. Vibrational temperatures were obtained from absorption measurements behind the incident shock waves. The strong dependence of absorption cross-sections in the O_2 Schumann-Runge bands on vibrational temperature was used to deduce vibrational temperature time-histories. Translational temperature and composition were then derived via 1-D energy and mass conservation laws. Since then, this work has gone on to become the crux of validation attempts for new thermochemical nonequilibrium models of oxygen. Unfortunately, this experimental data has large uncertainty due to limitations of the apparatus, particularly of the optical system. This makes the discrimination of one computational model against another hardly possible. However, comparison against the experimental profiles of vibrational temperature is still beneficial as a sanity check for a proposed set of kinetic rate coefficients.

Although Ibraguimova et al. report results for several initial pressure and velocity conditions, only three of these cases are simulated for their various degrees of nonequilibrium. The same three

shock cases studied in the 0-D adiabatic oxygen reservoir section are again chosen here. The initial fill pressures, p_{fill}, and incident shock velocities, u_{is}, for each case are provided in Table 3.7. For all cases, the initial composition is 100% O_2.

Table 3.7: Initial conditions for the test cases considered from Ibraguimova et al.'s [8] shock-tube experiments

Case	p_{fill} **(Torr)**	u_{is} **(km/s)**
LNEQ	2.0	3.07
MNEQ	1.0	3.95
HNEQ	0.8	4.44

Along with the QCT-ME calculations, the cases are also run using Park's two-temperature model for comparison. The post-shock temperature profiles predicted by the two computational models are plotted alongside the experimental measurements for the three shock cases in Fig. 3.31. The QCT-ME and Park model predictions are indicated by the black and blue dash-dot-dot profiles, respectively. The experimental results from Ibraguimova et al. are shown as square symbols with error bounds. The experimental error bounds are added as proposed by Ibraguimova et al. However, the recent investigation by Wysong et al. [83] argues that they could be up to 100% larger than what is suggested in the original publication.

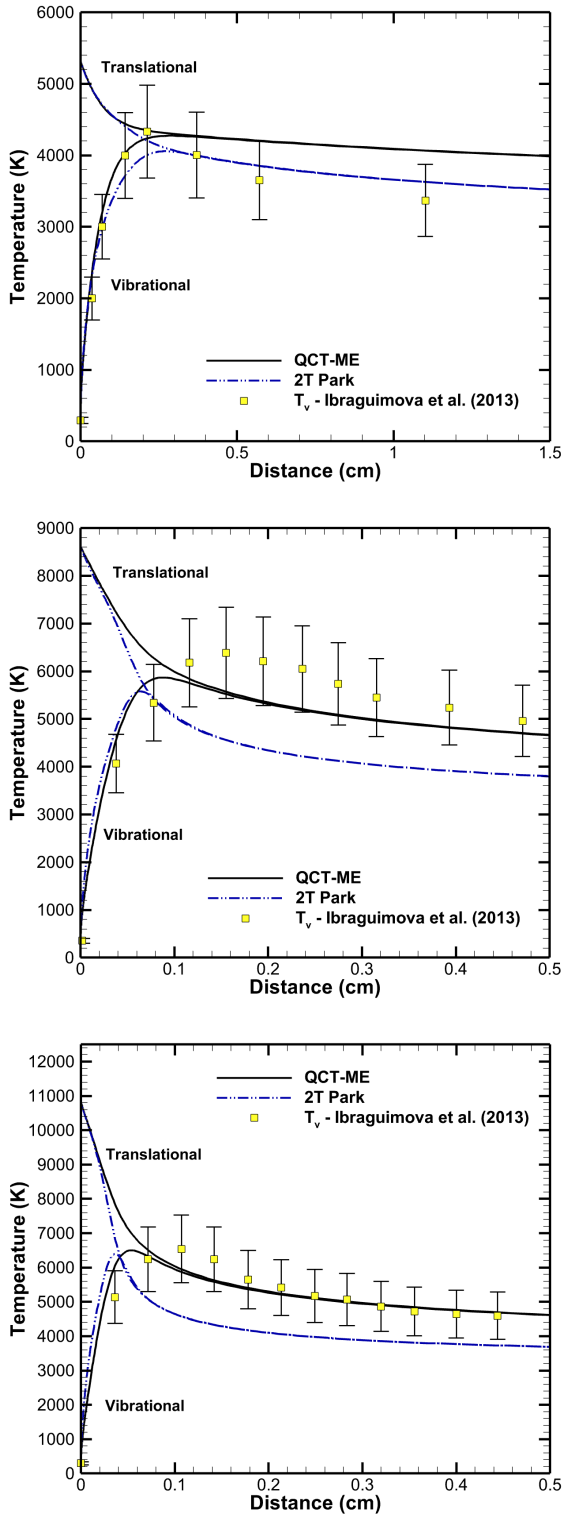

Figure 3.31: Post-normal shock temperature predictions in Ibraguimova et al.'s shock-tube experiments [8] (LNEQ, MNEQ and HNEQ from top to bottom).

For the LNEQ case, the two computational models agree reasonably well. While the present QCT-ME model leads to a better prediction of the vibrational temperature rise and peak, Park's model is in better agreement with the experimental results for the subsequent drop in temperature after the peak. In this lower temperature regime, the rather coarse assumptions of Park's two-temperature model, such as the constant vibration-dissociation coupling coefficient and controlling temperature of $T_a = \sqrt{TT_v}$, are expected to still be acceptable. With the rise of nonequilibrium in the system, however, the differences between the models become more apparent. The QCT-ME model leads to a much better prediction of the temperature profiles in the MNEQ and HNEQ cases. This includes closer estimates of the peak vibrational temperature and the spatial location of this peak. On the other hand, Park's model shows significantly faster equilibration of the vibrational and translational modes. There are two primary reasons for this: 1) the use of a constant vibration-dissociation coupling factor, which leads to an overprediction of the vibrational energy removed during dissociation, hence a lower peak of vibrational temperature, and 2) Park's model overestimates the level of endothermic dissociation in these high-temperature cases.

Although vibrational temperature comparisons are important for understanding the level of molecular excitation in a given system, they are not an exact evaluation of the accuracy of a predictive model. A more important comparison, which strongly affects the aerothermochemistry of the flow and gas-surface interactions, is that of flow composition, which is shown in Fig. 3.32 for the LNEQ and MNEQ cases and in Fig. 3.33 for the HNEQ case. In all three shock cases, a significantly faster rise in atomic oxygen mole fraction is observed when Park's two-temperature model is employed when compared to the QCT-ME model. Depending on the shock stand-off distance (which itself is dependent on thermodynamic properties such as temperature), employing the simplified Park model may result in a drastic overprediction of surface heat flux, as more atoms will recombine and release energy as they interact with the surface than that predicted by the QCT-ME model.

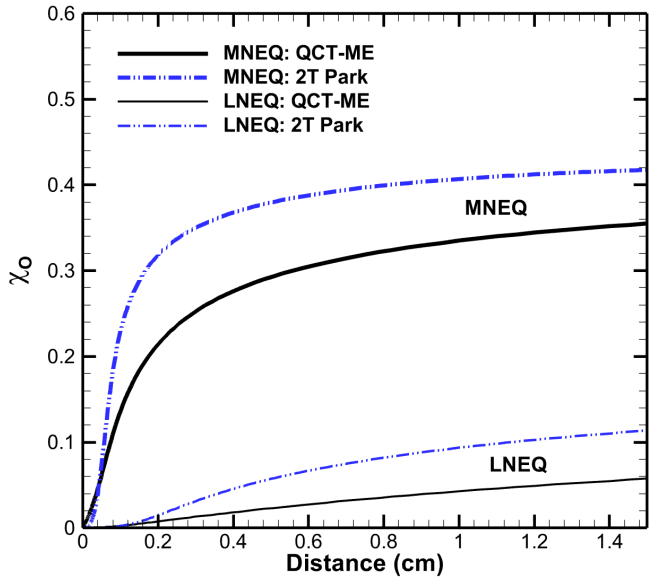

Figure 3.32: Post-normal shock atomic oxygen mole fraction predictions in Ibraguimova et al.'s shock-tube experiments [8] - LNEQ and MNEQ cases.

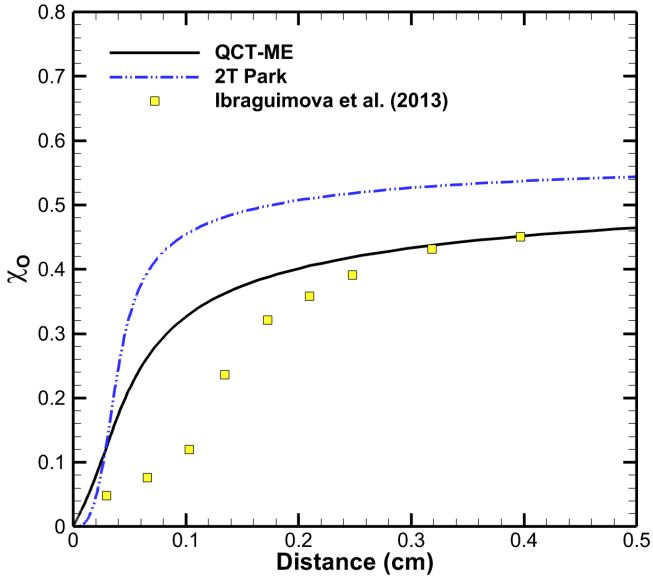

Figure 3.33: Post-normal shock atomic oxygen mole fraction predictions in Ibraguimova et al.'s shock-tube experiments [8] - HNEQ case.

3.4.3 Sharma and Gillespie (1991)

In the early 1990s, Sharma and Gillespie [10] conducted a set of pure nitrogen shock-tube experiments at NASA's EAST facility. Their work was motivated by the inability of multi-temperature models to reproduce even remotely similar predictions for vibrational temperature as those measured in the AVCO experiment [11] in the 1960s. Unlike the AVCO experiment, where radiation measurements of the first negative system of N_2^+ were used, Sharma and Gillespie measured radiation of the second positive system of N_2 ($C^3\Pi_u \rightarrow B^3\Pi_g$) to deduce vibrational and rotational temperatures at a single point behind the shock. Because vibrational energy transfer between N_2 and N_2^+ molecules may not be as efficient as energy transfer between electronic states of N_2, neutral and ion species could be at vastly different vibrational temperatures, thereby rendering measurements of electronic states of N_2 a better candidate for comparison with numerical calculations based on the ground state of N_2.

A number of studies have been undertaken to reproduce Sharma and Gillespie's experimental temperature measurements [84, 85]. However, these multi-temperature models consistently overpredicted the rate of vibrational relaxation when compared to the experiment. Kim and Boyd [9] were able to capture the vibrational and rotational temperature data points using a hybrid multi-temperature model, in which N_2–N interactions are rovibrationally-resolved. They argue that rotational nonequilibrium must be accounted for in these high-temperature shock cases to accurately model the thermochemical environment.

However, because vibrational relaxation times and dissociation rates based on accurate *ab-initio* calculations were not available at the time, Kim and Boyd used the Millikan and White correlation with $\sigma_v = 3\times10^{-18}$ cm^2 in the high-temperature correction for N_2–N_2 vibrational relaxation and the two-temperature N_2–N_2 Arrhenius dissociation rate of Baulch et al. [86] As shown by the dashed blue curve with square symbols in Fig. 3.3, the use of this collision limiting cross-section results in much slower relaxation times than any of the *ab-initio*-based vibrational relaxation times for the ground electronic state of N_2, or Appleton's experimental data, above approximately 8,000K. This collision limiting cross-section was used to ensure the N_2–N_2 rotational

relaxation times employed (based on a modified Park model [66]) did not become slower than the vibrational relaxation times at high temperatures.

When comparing the nonequilibrium dissociation rate coefficients with the present QCT ones, shown in Fig. 3.34 for T = 20,000K (the approximate initial post-shock translational temperature in the Sharma and Gillespie experiment), one sees that the Baulch et al. N_2–N_2 nonequilibrium dissociation rates are significantly lower than the corresponding QCT ones. It is noted, however, that the present nonequilibrium dissociation rates are computed assuming a Boltzmann distribution of vibrational states, so the true instantaneous dissociation rates in the ME model simulations are lower once significant dissociation begins. Also shown in the figure are the QCT rate coefficient coefficients of Chaudhry [42] as a verification of the present results.

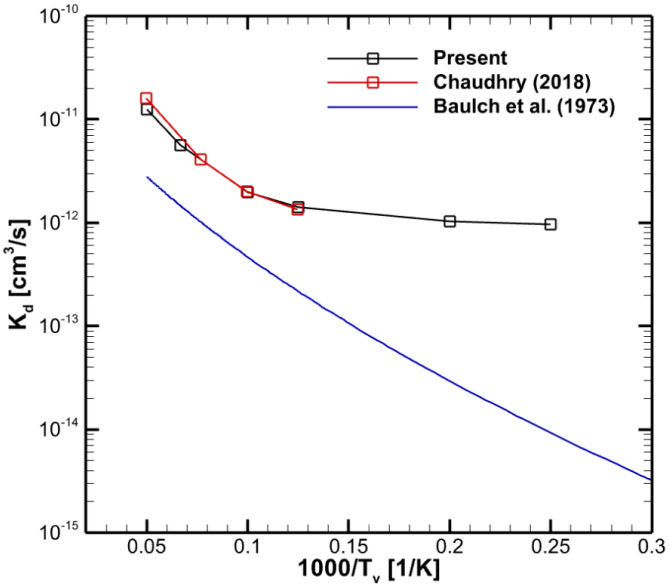

Figure 3.34: Nonequilibrium N_2–N_2 dissociation rate coefficients, T = 20,000K.

With this understanding of how present vibrational relaxation times and dissociation rates compare to those used by Kim and Boyd, Sharma and Gillespie's experiment is numerically simulated using the present vibrational-specific ME model for two model cases: 1) using the original QCT

bound-bound and bound-free rate coefficients, and 2) using bound-bound and bound-free rate coefficients which have been linearly scaled at each integration step to approximately match the N_2–N_2 vibrational relaxation times and dissociation rates used by Kim and Boyd. For this experiment, the freestream temperature and pressure are 300K and 1.0 torr, respectively, and the freestream velocity is 6.2 km/s.

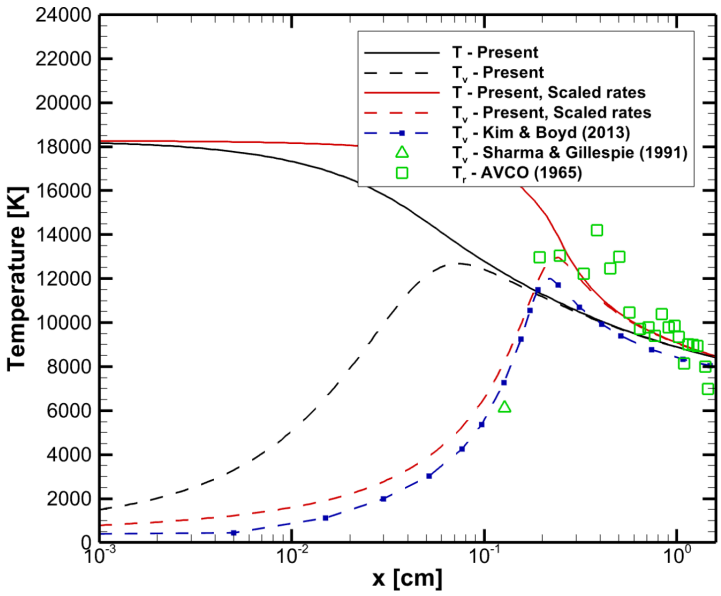

Figure 3.35: Comparison of the present model's temperature predictions to Kim and Boyd[9] and the shock-tube data of Sharma and Gillespie [10] and Allen [11].

The resulting temperature profiles are shown in Fig. 3.35. Only the T_v curve from Kim and Boyd is plotted for readability. The present model predicts much faster excitation and dissociation than Kim and Boyd's model and vastly overpredicts Sharma and Gillespie's vibrational temperature experimental data point. However, the model based on the linearly scaled rate coefficients is very similar to that of Kim and Boyd and agreement is good between experiment and computation. Although this scaling of rate coefficients is somewhat crude, this comparison, along with those to the DMS method in the previous sections, show that the inability of the present

vibrational-specific model to accurately capture Sharma and Gillespie's data point does not lie in the translational-rotational equilibrium assumption. Rather, Kim and Boyd were likely able to obtain good experimental agreement because of their choice of a very small collision limiting cross-section and a rotational relaxation model which predicts relaxation times much slower than either the Parker model [87] or those of Jo et al. [88], which are based on the most recent *ab-initio* QCT calculations.

The question remains then as to why the present model cannot accurately reproduce the vibrational temperature of N_2 ground state in the shock tube experiment. Recalling again that Sharma and Gillespie deduced vibrational temperature from radiation measurements of the electronically excited C-state, one has to consider whether the vibrational modes of excited electronic states are equilibrated with the ground state.

For the high freestream velocity considered in the Sharma and Gillespie experiment (6.2 km/s), the primary means by which N_2 is excited to higher electronic states is through collisions with electrons [89], although charge exchange in N_2^+–N collisions and excitation due to heavy particle impact may also contribute to a lesser degree. Therefore, understanding the evolution of electron concentration in the flow, what vibrational states these excited electronic states are being formed in, and how vibrational energy transfer occurs between ground and excited electronic states may provide insight into this matter. It is also noted that endothermic ionization processes affect temperature, and hence decrease relaxation times, although the extent of which is likely small relative to the large disagreement between the present numerical model and experiment. It is therefore concluded that experimental techniques which can probe and obtain accurate data from the ground electronic state of N_2 are highly desired to resolve these uncertainties (although it is recognized that issues arise when trying to measure such 'dark' states).

3.5 First post-shock simulations of the 5-species system of *ab-initio* accuracy

The following two subsections present the first isothermal and adiabatic reservoir simulations of the 5-species air system using rate coefficients of *ab-initio* only. For comparison, calculations are also made using Park's multi-temperature model.

3.5.1 0-D isothermal reservoir cases

0-D 5-species isothermal air heat bath simulations are completed considering all interactions specified in Table 1 of Ref. [43]. For these calculations, the initial number density is set to 2×10^{18} cm^{-3}, with 80% N_2 and 20% O_2 by mole fraction. Vibrational states are initialized to a Boltzmann distribution at 300 K, and the translational-rotational temperature is fixed at 10,000K.

The instantaneous mole fraction predictions from both computational models are shown in Fig. 3.36. Because upper vibrational states of O_2 are quickly overpopulated compared to a Boltzmann distribution at the instantaneous vibrational temperature, a greater amount of atomic oxygen is present in the vibrational-specific model predictions at early times. However, the MT model dissociation rates soon become larger than the corresponding QCT dissociation rates due to the faster vibrational relaxation times of diatom-diatom collisions in the Millikan and White correlation when compared to the QCT relaxation times (see Fig.'s 3.6 and 3.3). Once this occurs, the atomic oxygen concentration predicted by the MT model quickly surpasses the QCT model, and the system reaches equilibrium much more quickly due to efficient energy transfer in collision events with oxygen radicals.

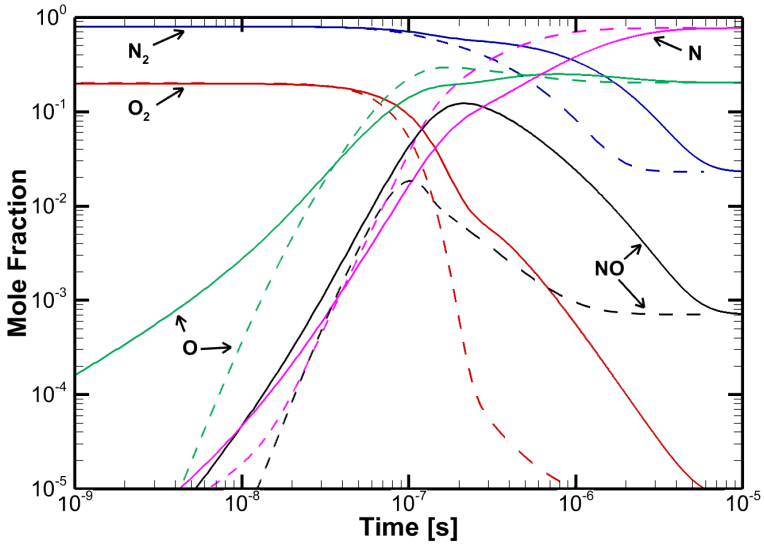

Figure 3.36: Mole fraction predictions in an isothermal reservoir of the 5-species air system at 10,000K. Solid profiles correspond to the present predictions, and dashed profiles correspond to Park's MT model predictions.

An important aspect to note from Fig. 3.36 is that the peak formation of nitric oxide is greatly underpredicted when Park's MT model is employed. The QCT model predicts a peak nitric oxide mole fraction which is approximately 6.6 times greater than the MT model. Su et al. [32] noted similar discrepancies between models in their one-dimensional state-to-state and MT model comparisons. The inability of the MT model to accurately capture the presence of nitric oxide in the flow could potentially result in dramatic underpredictions of radiative heat flux, as the vibrationally 'hot' nitric oxide molecules can readily jump to excited electronic states.

The corresponding molecular vibrational temperatures are shown in Fig. 3.37. Of particular interest is the evolution of nitric oxide. The nitric oxide molecules are formed vibrationally 'hot', and their vibrational temperature peaks above the equilibrium temperature. This peak in vibrational temperature occurs slightly before its peak in concentration. Bose and Candler [90, 91] studied the kinetics of nitric oxide formation and showed that this phenomenon occurs because of the efficient channeling of translational energy to the vibrational mode for the first Zeldovich mechanism when the vibrational temperature is lower than the translational temperature and the exothermicity of the

second Zeldovich mechanism.

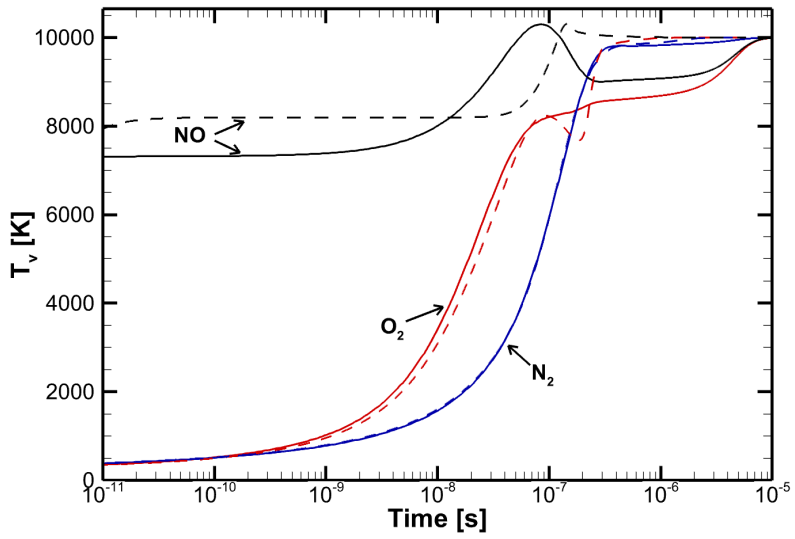

Figure 3.37: Vibrational temperature predictions in an isothermal reservoir of the 5-species air system at 10,000K. Solid profiles correspond to the present predictions, and dashed profiles correspond to Park's MT model predictions.

The vibrational energy distributions of each molecule are extracted from the vibrational-specific ME model simulation at three time stamps to further assess the evolution of the system at the microscopic level. The results are shown in Fig. 3.38. At early times, the upper vibrational states of N_2 and O_2 quickly become overpopulated due to the ease of energy transfer between these closely spaced vibrational states. Once the molecules are sufficiently vibrationally excited, dissociation begins to occur, and the tails of the vibrational state distributions become depleted compared to a Boltzmann distribution at the instantaneous vibrational temperature because upper vibrational states are preferentially dissociated. In contrast to N_2 and O_2, the nonequilibrium distributions of nitric oxide are overpopulated at vibrational states greater than the average vibrational energy of NO for nearly the entire simulation due to the preferential formation of nitric oxide molecules to these excited energy levels. The level of NO formation in hypersonic flows is often an important parameter in accurately determining radiative heat fluxes (excited NO molecules can readily jump

to and from excited electronic states). Accurately capturing the formation of these vibrationally hot nitric oxide molecules is potentially a critical aspect that should be considered when choosing a thermochemical nonequilibrium air model.

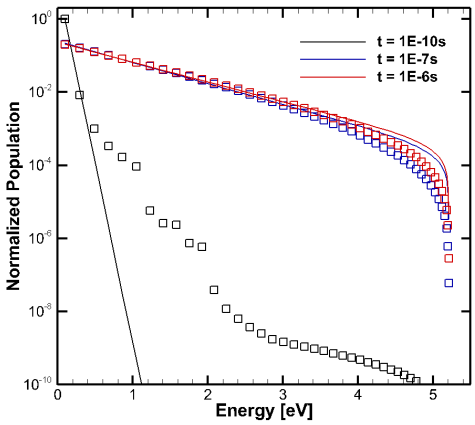

(a) O_2

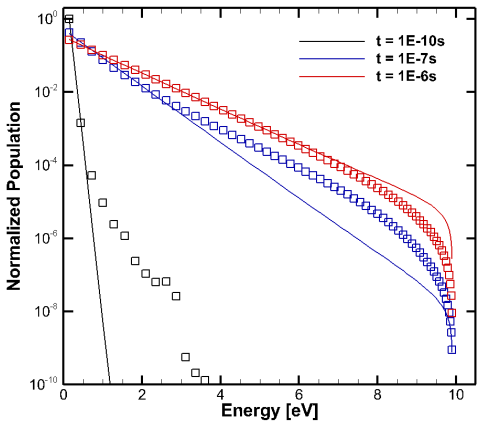

(b) N_2

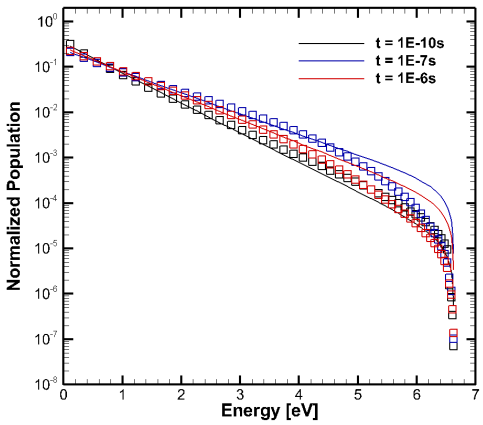

(c) NO

Figure 3.38: Instantaneous vibrational state distributions in an isothermal reservoir of the 5-species air system, T = 10,000K. Solid lines designate Boltzmann distributions at T_v and symbols designate nonequilibrium distributions.

3.5.2 0-D adiabatic reservoir cases

Fig.'s 3.39 and 3.40 show the composition and temperature profiles for an adiabatic reservoir with an initial translational temperature of 15,000 K and an initial vibrational temperature of 300 K, respectively. The system is initialized with a number density of 1×10^{19} cm^{-3}, of which 79% is N_2 and 21% is O_2, by mole fraction. These initial conditions conform with those of the Hypersonic Non-Equilibrium Comparison (HyNECC) initiative [92] (the HyNECC paper on air cases, "Kinetic and Continuum Modeling of High Temperature Air Relaxation", is currently under review).

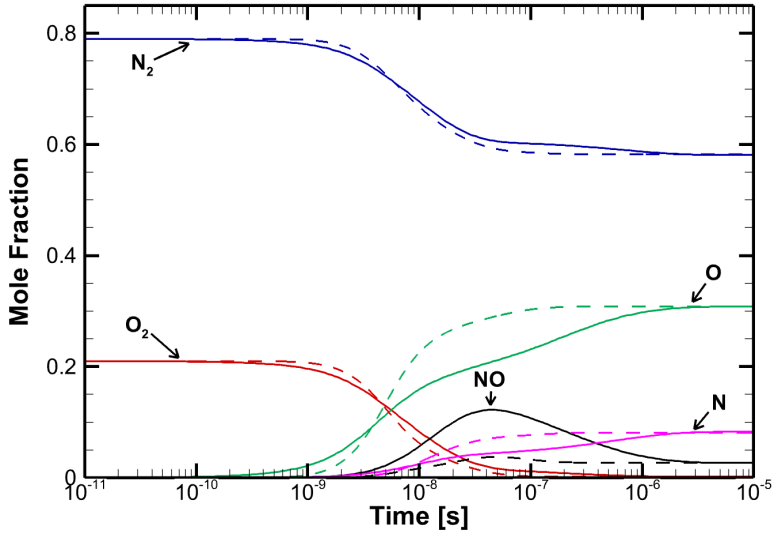

Figure 3.39: Mole fraction predictions in an adiabatic reservoir of the 5-species air system, T^0 = 15,000 K. Solid profiles correspond to the present predictions, and dashed profiles correspond to Park's MT model predictions.

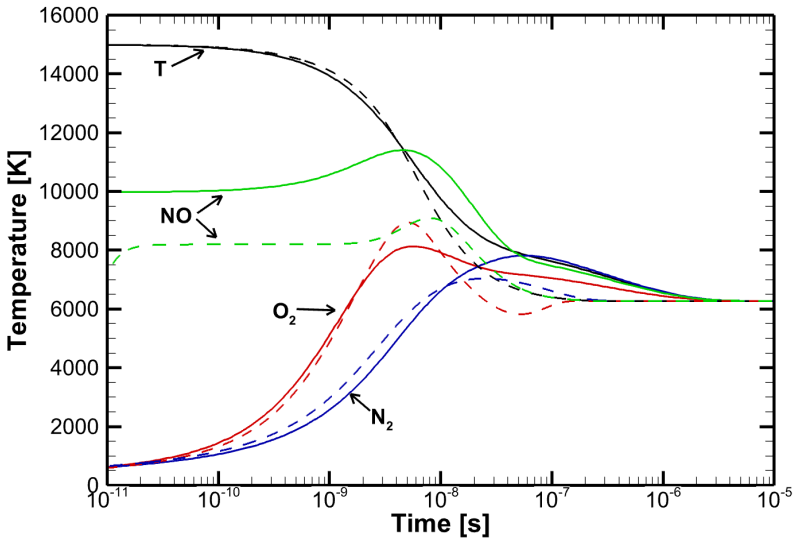

Figure 3.40: Translational and vibrational temperature predictions in an adiabatic reservoir of the 5-species air system, T^0 = 15,000 K. Solid profiles correspond to the present predictions, and dashed profiles correspond to Park's MT model predictions. Translational temperature is denoted by 'T', and vibrational temperatures are denoted by the molecular species name.

Similarities between the isothermal and adiabatic simulations can be noted in both the mole fraction and temperature plots. The vibrational temperature of nitric oxide instantly jumps to a much larger value than the O_2 and N_2 temperatures and eclipses the translational temperature before settling to the equilibrium value. The peak mole fraction of NO for the vibrational-specific model is 0.12, whereas it is only 0.04 for Park's MT model. Because the DMS method is far from achieving full air simulations, these vibrational-specific model results provide a high-fidelity metric that can be used to analyze new thermochemistry models of air.

4. SUMMARY AND CONCLUSIONS

Vibrational-resolved models describing the thermo-chemical relaxation of air species in post-shock conditions using only *ab-initio*-based methods are presented. State-to-state rate coefficients of vibrational excitation and dissociation are calculated using the QCT method on high-fidelity potential energy surfaces. To reduce the computational expense of computing the diatom-diatom rate coefficients, two assumptions are made: 1) the translational and rotational modes are equilibrated immediately behind the shock, and 2) all collisions occur with a projectile molecule in the lowest few vibrational states. The kinetic air database is implemented into a system of master equations and coupled with the conservation laws to simulate a series of computational experiments, including isothermal and adiabatic reservoirs and the shock-tube experiments of and Streicher et al. [7], Ibraguimova et al. [8], and Sharma and Gillespie [10].

Good agreement between the present vibrational-specific model and the DMS method by way of 0-D adiabatic reservoir binary mixture species composition and vibrational temperature predictions suggests that atomic radicals' ability to quickly redistribute energy in molecular collisions decreases the importance of the grouping strategy employed. The ability of the vibrational-specific model to capture the primary characteristics of nonequilibrium excitation and dissociation is encouraging, as rovibrationally-resolving such problems quickly becomes intractable in the presence of many species in multiple dimensions.

Large differences were noted between the present master equation model and various multi-temperature models, including Park's model and the Macheret-Fridman dissociation model, in terms of vibrational temperature predictions and species compositions in post-incident and post-reflected shock environments, where the former greatly outperformed the simplified models. Heating loads are particularly sensitive to species compositions and temperature gradients, thus accurately determining the post-shock state is crucial for adequately sizing a hypersonic body's (trans-atmospheric vehicle, cruise missile, reentry capsule, etc.) thermal protection system.

Results from modeling the shock-tube experiments of Streicher et al. [7] suggest that the frozen

vibrational mode assumption may lead to non-negligible errors in estimating initial post-reflected shock conditions. Accounting for relaxation behind the incident shock and the unsteady nature of the reflected shock-wave itself may be necessary to obtain such quantities. This phenomenon is exacerbated when the test gas considered is not diluted with an inert species, such as argon, as additional energy is required to vibrationally excite and dissociate the molecules in the flow. Model validation hinges on the reliability of experimental results, thus it is important to keep such factors in mind when post-processing raw experimental data and when numerically modeling shock-tube experiments.

Comparisons to Sharma and Gillespie's experiment indicate that vibrational relaxation in the N_2 ground electronic state occurs substantially faster than in the excited electronic states observed in experiments. It is believed that the source of discrepancy between experimental and computational vibrational temperature predictions does not lie in the assumption of transitional-rotational equilibrium made in this work, given the good agreement between present results and the DMS model.

For the first time, post-shock simulations of the full 5-species air system are presented with *ab-initio* accuracy. It is shown that Park's model greatly underpredicts the formation of nitric oxide in the cases considered. The inability of the multi-temperature model to accurately capture the presence of nitric oxide could result in dramatic underpredictions in radiative heat flux calculations, as the vibrationally 'hot' nitric oxide molecules can readily jump to excited electronic states. Because the present vibrationally-resolved model is capable of capturing the inherent non-Boltzmann natures of the molecules within these gas systems, the results obtained and the physics discovered throughout the course of this work provide a high-fidelity metric for future thermo-chemical nonequilibrium models of air relaxation.

4.1 Further study

This work helps lay the foundation for prospective detailed models of aerothermochemistry. Although this work focuses on numerically studying simplified post-shock environments, important high-temperature physics, which are relevant to theorists and experimentalists alike, were

discovered. As the next step, the master equation models developed in this work could be effectively coupled to an efficient multi-dimensional fluid solver to simulate more complex hypersonic geometries. An advantage of the master equation approach is that important physical features of a real gas flow, such as transport phenomena or gas-surface interactions, may be added to the model at a minimal cost. It will certainly be an exciting time in the hypersonic community when the first full-scale vehicle simulations of *ab-initio* accuracy are achieved.

REFERENCES

[1] D. A. Andrienko, "The importance of O_3 excited potential energy surfaces in O_2–O high-temperature kinetics," *The Journal of Chemical Physics*, vol. 152, no. 4, p. 044305, 2020.

[2] P. Valentini, T. E. Schwartzentruber, J. D. Bender, I. Nompelis, and G. V. Candler, "Direct molecular simulation of nitrogen dissociation based on an ab initio potential energy surface," *Physics of Fluids*, vol. 27, no. 8, p. 086102, 2015.

[3] P. Valentini, T. E. Schwartzentruber, J. D. Bender, and G. V. Candler, "Dynamics of nitrogen dissociation from direct molecular simulation," *Physical Review Fluids*, vol. 1, no. 4, p. 043402, 2016.

[4] E. Torres and T. E. Schwartzentruber, "Direct molecular simulation of nitrogen dissociation under adiabatic postshock conditions," *Journal of Thermophysics and Heat Transfer*, pp. 1–15, 2020.

[5] T. E. Schwartzentruber, M. S. Grover, and P. Valentini, "Direct molecular simulation of nonequilibrium dilute gases," *Journal of Thermophysics and Heat Transfer*, vol. 32, no. 4, pp. 892–903, 2018.

[6] E. Torres and T. E. Schwartzentruber, "Direct molecular simulation of dissociating oxygen under adiabatic and normal shock wave conditions," in *AIAA Scitech 2021 Forum*, p. 0318, 2021.

[7] J. W. Streicher, A. Krish, and R. K. Hanson, "Coupled vibration-dissociation time-histories and rate measurements in shock-heated, nondilute o2 and o2–ar mixtures from 6000 to 14 000 k," *Physics of Fluids*, vol. 33, no. 5, p. 056107, 2021.

[8] L. Ibraguimova, A. Sergievskaya, V. Y. Levashov, O. Shatalov, Y. V. Tunik, and I. Zabelinskii, "Investigation of oxygen dissociation and vibrational relaxation at temperatures 4000–10 800 K," *Journal of Chemical Physics*, vol. 139, no. 3, p. 034317, 2013.

[9] J. G. Kim and I. D. Boyd, "State-resolved master equation analysis of thermochemical nonequilibrium of nitrogen," *Chemical Physics*, vol. 415, pp. 237–246, 2013.

[10] S. P. Sharma and W. Gillespie, "Nonequilibrium and equilibrium shock front radiation measurements," *Journal of Thermophysics and Heat transfer*, vol. 5, no. 3, pp. 257–265, 1991.

[11] R. A. Allen, "Nonequilibrium shock front rotational, vibrational and electronic temperature measurements," *Journal of Quantitative Spectroscopy and Radiative Transfer*, vol. 5, no. 3, pp. 511–523, 1965.

[12] C. on the Planetary Science Decadal Survey, *Vision and Voyages: For Planetary Science in the Decade 2013-2022*. National Academies Press, 2011.

[13] J. Szalay, P. Pokornỳ, S. Bale, E. Christian, K. Goetz, K. Goodrich, M. Hill, M. Kuchner, R. Larsen, D. Malaspina, *et al.*, "The near-sun dust environment: Initial observations from parker solar probe," *The Astrophysical Journal Supplement Series*, vol. 246, no. 2, p. 27, 2020.

[14] K. Edquist, "Computations of viking lander capsule hypersonic aerodynamics with comparisons to ground and flight data," in *AIAA Atmospheric Flight Mechanics Conference and Exhibit*, p. 6137, 2006.

[15] F. S. Milos, "Galileo probe heat shield ablation experiment," *Journal of Spacecraft and Rockets*, vol. 34, no. 6, pp. 705–713, 1997.

[16] H. Duan and P. Li, "Progress in control approaches for hypersonic vehicle," *Science China Technological Sciences*, vol. 55, no. 10, pp. 2965–2970, 2012.

[17] B. A. Rankin, M. L. Fotia, A. G. Naples, C. A. Stevens, J. L. Hoke, T. A. Kaemming, S. W. Theuerkauf, and F. R. Schauer, "Overview of performance, application, and analysis of rotating detonation engine technologies," *Journal of Propulsion and Power*, vol. 33, no. 1, pp. 131–143, 2017.

[18] E. T. Curran, "Scramjet engines: the first forty years," *Journal of Propulsion and Power*, vol. 17, no. 6, pp. 1138–1148, 2001.

[19] O. Uyanna and H. Najafi, "Thermal protection systems for space vehicles: A review on technology development, current challenges and future prospects," *Acta Astronautica*, 2020.

[20] T. K. West IV and S. Hosder, "Uncertainty quantification of hypersonic reentry flows with sparse sampling and stochastic expansions," *Journal of Spacecraft and Rockets*, vol. 52, no. 1, pp. 120–133, 2015.

[21] G. V. Candler, "Rate effects in hypersonic flows," *Annual Review of Fluid Mechanics*, vol. 51, pp. 379–402, 2019.

[22] M. E. Holloway, K. M. Hanquist, and I. D. Boyd, "Effect of thermochemistry modeling on hypersonic flow over a double cone," in *AIAA Scitech 2019 Forum*, p. 2281, 2019.

[23] J. Ray, S. Kieweg, D. Dinzl, B. Carnes, V. G. Weirs, B. Freno, M. Howard, T. Smith, I. Nompelis, and G. V. Candler, "Estimation of inflow uncertainties in laminar hypersonic double-cone experiments," *AIAA journal*, vol. 58, no. 10, pp. 4461–4474, 2020.

[24] S. Gu and H. Olivier, "Capabilities and limitations of existing hypersonic facilities," *Progress in Aerospace Sciences*, vol. 113, p. 100607, 2020.

[25] C. Park, "Review of chemical-kinetic problems of future NASA missions, I: Earth entries," *Journal of Thermophysics and Heat Transfer*, vol. 7, no. 3, pp. 385–398, 1993.

[26] C. Park, "The limits of two-temperature kinetic model in air," in *48th AIAA Aerospace Sciences Meeting Including the New Horizons Forum and Aerospace Exposition*, p. 911, 2010.

[27] D. A. Andrienko and I. D. Boyd, "Rovibrational energy transfer and dissociation in O_2–O collisions," *Journal of Chemical Physics*, vol. 144, no. 10, p. 104301, 2016.

[28] G. Bellas-Chatzigeorgis, P. F. Barbante, and T. E. Magin, "Energy accommodation coefficient calculation methodology using state-to-state catalysis applied to hypersonic flows," *AIAA Journal*, vol. 58, no. 1, pp. 278–290, 2020.

[29] F. Bariselli, E. Torres, and T. E. Magin, "State-specific catalytic recombination boundary condition for DSMC methods in aerospace applications," in *AIP Conference Proceedings*, vol. 1786, p. 190009, AIP Publishing LLC, 2016.

[30] G. Bellas-Chatzigeorgis, P. F. Barbante, and T. E. Magin, "Development of detailed chemistry models for boundary layer catalytic recombination," in *8th European Symposium on Aerothermodynamics for Space Vehicle*, pp. 1–8, 2015.

[31] M. Panesi, R. L. Jaffe, D. W. Schwenke, and T. E. Magin, "Rovibrational internal energy transfer and dissociation of $N_2(^1\Sigma_g^+)$–$N(^4S_u)$ system in hypersonic flows," *The Journal of chemical physics*, vol. 138, no. 4, p. 044312, 2013.

[32] W. Su, D. Bruno, and Y. Babou, "State-specific modeling of vibrational relaxation and nitric oxide formation in shock-heated air," *Journal of Thermophysics and Heat Transfer*, vol. 32, no. 2, pp. 337–352, 2017.

[33] I. V. Adamovich, S. O. Macheret, J. W. Rich, and C. E. Treanor, "Vibrational relaxation and dissociation behind shock waves. Part 1-Kinetic rate models.," *AIAA journal*, vol. 33, no. 6, pp. 1064–1069, 1995.

[34] M. Panesi and A. Lani, "Collisional radiative coarse-grain model for ionization in air," *Physics of Fluids*, vol. 25, no. 5, p. 057101, 2013.

[35] G. V. Candler, P. K. Subbareddy, and I. Nompelis, "Decoupled implicit method for aerothermodynamics and reacting flows," *AIAA journal*, vol. 51, no. 5, pp. 1245–1254, 2013.

[36] N. Singh and T. Schwartzentruber, "Consistent kinetic–continuum dissociation model i. kinetic formulation," *The Journal of Chemical Physics*, vol. 152, no. 22, p. 224302, 2020.

[37] R. S. Chaudhry, N. Singh, M. S. Grover, T. E. Schwartzentruber, and G. V. Candler, "Implementation of a nitrogen chemical kinetics model based on ab-initio data for hypersonic CFD," in *2018 Joint Thermophysics and Heat Transfer Conference*, 2018.

[38] H. Luo, A. A. Alexeenko, and S. O. Macheret, "Assessment of classical impulsive models of dissociation in thermochemical nonequilibrium," *Journal of Thermophysics and Heat Transfer*, vol. 32, no. 4, pp. 861–868, 2018.

[39] R. C. Millikan and D. R. White, "Systematics of vibrational relaxation," *Journal of Chemical Physics*, vol. 39, no. 12, p. 3209, 1963.

[40] R. Schwartz, Z. Slawsky, and K. Herzfeld, "Calculation of vibrational relaxation times in gases," *The Journal of Chemical Physics*, vol. 20, no. 10, pp. 1591–1599, 1952.

[41] D. G. Truhlar and J. T. Muckerman, "Reactive scattering cross sections III: quasiclassical and semiclassical methods," in *Atom-Molecule Collision Theory*, pp. 505–566, Springer, 1979.

[42] R. S. Chaudhry, J. D. Bender, T. E. Schwartzentruber, and G. V. Candler, "Quasiclassical trajectory analysis of nitrogen for high-temperature chemical kinetics," *Journal of Thermophysics and Heat Transfer*, vol. 32, no. 4, pp. 833–845, 2018.

[43] A. J. Fangman and D. Andrienko, "A state-to-state and multi-temperature study of air thermochemistry," in *AIAA Scitech 2021 Forum*, p. 0316, 2021.

[44] J. D. Bender, P. Valentini, I. Nompelis, Y. Paukku, Z. Varga, D. G. Truhlar, T. Schwartzentruber, and G. V. Candler, "An improved potential energy surface and multi-temperature quasiclassical trajectory calculations of N_2 + N_2 dissociation reactions," *The Journal of chemical physics*, vol. 143, no. 5, p. 054304, 2015.

[45] Y. Paukku, Z. Varga, and D. G. Truhlar, "Potential energy surface of triplet O_4," *The Journal of Chemical Physics*, vol. 148, no. 12, p. 124314, 2018.

[46] D. A. Andrienko and I. D. Boyd, "State-specific dissociation in O_2–O_2 collisions by quasiclassical trajectory method," *Chemical Physics*, vol. 491, pp. 74–81, 2017.

[47] A. Varandas and A. Pais, "Double many-body expansion potential energy surface for $O_4(^3A)$, dynamics of the $O(^3P)$+ $O_3(^1A_1)$ reaction, and second virial coefficients of molecular oxygen," in *Theoretical and Computational Models for Organic Chemistry*, pp. 55–78, Springer, 1991.

[48] M. S. Grover, E. Torres, and T. E. Schwartzentruber, "Direct molecular simulation of internal energy relaxation and dissociation in oxygen," *Physics of Fluids*, vol. 31, no. 7, p. 076107, 2019.

[49] R. Chaudhry, "Modeling and analysis of chemical kinetics for hypersonic flows in air," 2018.

[50] F. Esposito, I. Armenise, G. Capitta, and M. Capitelli, "O+O_2 state-to-state vibrational relaxation and dissociation rates based on quasiclassical calculations," *Chemical Physics*, vol. 351, no. 1-3, pp. 91–98, 2008.

[51] I. Armenise and F. Esposito, "N_2, O_2, NO state-to-state vibrational kinetics in hypersonic boundary layers: The problem of rescaling rate coefficients to uniform vibrational ladders," *Chemical Physics*, vol. 446, pp. 30–46, 2015.

[52] J. Grinstead, M. Wilder, J. Olejniczak, D. Bogdanoff, G. Allen, K. Dang, and M. Forrest, "Shock-heated air radiation measurements at lunar return conditions," in *46th AIAA Aerospace Sciences Meeting and Exhibit*, p. 1244, 2008.

[53] C. K. Law, "Combustion at a crossroads: Status and prospects," *Proceedings of the Combustion Institute*, vol. 31, no. 1, pp. 1–29, 2007.

[54] S. F. Gimelshein and I. J. Wysong, "Impact of the ionization reaction set in nonequilibrium hypersonic air flows," *AIAA Journal*, vol. 58, no. 3, pp. 1255–1265, 2020.

[55] P. O. Dral, "Quantum chemistry in the age of machine learning," *The journal of physical chemistry letters*, vol. 11, no. 6, pp. 2336–2347, 2020.

[56] A. W. Irwin, "Refined diatomic partition functions. I-calculational methods and H_2 and CO results," *Astronomy and Astrophysics*, vol. 182, pp. 348–358, 1987.

[57] R. A. Strehlow and A. Cohen, "Limitations of the reflected shock technique for studying fast chemical reactions and its application to the observation of relaxation in nitrogen and oxygen," *The Journal of Chemical Physics*, vol. 30, no. 1, pp. 257–265, 1959.

[58] J. Appleton, "Shock-tube study of the vibrational relaxation of nitrogen using vacuum-ultraviolet light absorption," *The Journal of Chemical Physics*, vol. 47, no. 9, pp. 3231–3240, 1967.

[59] R. K. Hanson and D. F. Davidson, "Recent advances in laser absorption and shock tube methods for studies of combustion chemistry," *Progress in Energy and Combustion Science*, vol. 44, pp. 103–114, 2014.

[60] J. Toennies and E. Greene, "Dissociation energies of carbon monoxide and nitrogen from reflected shock wave studies," *The Journal of Chemical Physics*, vol. 26, no. 3, pp. 655–662, 1957.

[61] K. M. Hanquist, R. S. Chaudhry, I. D. Boyd, J. Streicher, A. Krish, and R. Hanson, "Detailed thermochemical modeling of O_2–Ar mixtures in reflected shock tube flows," in *AIAA AVIATION 2020 FORUM*, p. 3275, 2020.

[62] J. D. Anderson, *Modern compressible flow: with historical perspective*. McGraw-Hill, 3 ed., 2003.

[63] F. M. White and J. Majdalani, *Viscous fluid flow*, vol. 3. McGraw-Hill New York, 2006.

[64] M. F. Campbell, T. Parise, A. M. Tulgestke, R. M. Spearrin, D. F. Davidson, and R. K. Hanson, "Strategies for obtaining long constant-pressure test times in shock tubes," *Shock Waves*, vol. 25, no. 6, pp. 651–665, 2015.

[65] C. Park, *Nonequilibrium hypersonic aerothermodynamics*. Wiley, 1989.

[66] C. Park, "Rotational relaxation of N_2 behind a strong shock wave," *Journal of Thermophysics and Heat Transfer*, vol. 18, no. 4, pp. 527–533, 2004.

[67] R. Macdonald, R. Jaffe, D. Schwenke, and M. Panesi, "Construction of a coarse-grain quasi-classical trajectory method. I. theory and application to N_2–N_2 system," *The Journal of chemical physics*, vol. 148, no. 5, p. 054309, 2018.

[68] R. Jaffe, D. Schwenke, and G. Chaban, "Vibrational and rotational excitation and dissociation in N_2–N_2 collisions from accurate theoretical calculations," 10th AIAA/ASME Joint Thermophysics and Heat Transfer Conference, AIAA Paper 2010-4517, June 2010.

[69] M. S. Grover, N. Singh, T. E. Schwartzentruber, and R. L. Jaffe, "Dissociation and internal excitation of molecular nitrogen due to N_2-N collisions using direct molecular simulation," in *55th AIAA Aerospace Sciences Meeting*, p. 0660, 2017.

[70] R. Jaffe, D. Schwenke, G. Chaban, and W. Huo, "Vibrational and rotational excitation and relaxation of nitrogen from accurate theoretical calculations," in *46th AIAA Aerospace Sciences Meeting and Exhibit*, p. 1208, 2008.

[71] G. Chaban, R. Jaffe, D. Schwenke, and W. Huo, "Dissociation cross sections and rate coefficients for nitrogen from accurate theoretical calculations," in *46th AIAA Aerospace Sciences Meeting and Exhibit*, p. 1209, 2008.

[72] R. L. Jaffe, M. Grover, S. Venturi, D. W. Schwenke, P. Valentini, T. E. Schwartzentruber, and M. Panesi, "Comparison of potential energy surface and computed rate coefficients for N_2 dissociation," *Journal of thermophysics and heat transfer*, vol. 32, no. 4, pp. 869–881, 2018.

[73] D. Kewley and H. Hornung, "Free-piston shock-tube study of nitrogen dissociation," *Chemical Physics Letters*, vol. 25, no. 4, pp. 531–536, 1974.

[74] M. Grover, "Direct molecular simulation of nitrogen and oxygen at hypersonic conditions," 2018.

[75] R. Macdonald, M. Grover, T. E. Schwartzentruber, and M. Panesi, "Construction of a coarse-grain quasi-classical trajectory method. II. comparison against the direct molecular simulation method," *The Journal of chemical physics*, vol. 148, no. 5, p. 054310, 2018.

[76] R. Chaudhry, *Modeling and Analysis of Chemical Kinetics for Hypersonic Flows in Air*. University of Minnesota Digital Conservancy, 2018.

[77] M. Lino da Silva, B. Lopez, V. Guerra, and J. Loureiro, "A multiquantum state-to-state model for the fundamental states of air: the stellar database," in *ESA Special Publication*, vol. 714, 2012.

[78] O. Shatalov, "Molecular dissociation of oxygen in the absence of vibrational equilibrium," *Combustion, Explosion, and Shock Waves*, vol. 9, no. 5, pp. 610–613, 1973.

[79] E. Torres and T. E. Schwartzentruber, "Direct molecular simulation of dissociating nitrogen in an adiabatic reactor," in *AIAA Scitech 2019 Forum*, p. 1049, 2019.

[80] R. L. Macdonald, R. L. Jaffe, D. W. Schwenke, and M. Panesi, "Construction of a coarse-grain quasi-classical trajectory method. I. theory and application to N_2–N_2 system," *The Journal of Chemical Physics*, vol. 148, no. 5, p. 054309, 2018.

[81] N. Johannesen, G. Bird, and H. Zienkiewicz, "Theoretical and experimental investigations of the reflexion of normal shock waves with vibrational relaxation," *Journal of Fluid Mechanics*, vol. 30, no. 1, pp. 51–64, 1967.

[82] L. L. Presley and R. K. Hanson, "Numerical solutions of reflected shock-wave flowfields with nonequilibrium chemical reactions," *AIAA Journal*, vol. 7, no. 12, pp. 2267–2273, 1969.

[83] I. J. Wysong, S. F. Gimelshein, N. E. Bykova, O. P. Shatalov, and I. E. Zabelinski, "Impact of flow non-equilibrium in oxygen shock absorption analysis," *AIP Conference Proceedings*, vol. 2132, no. 1, p. 180008, 2019.

[84] S. Moreau, P.-Y. Bourquin, D. Chapman, and R. MacCormack, "Numerical simulation of Sharma's shock-tube experiment," in *31st Aerospace Sciences Meeting*, p. 273, 1993.

[85] A. Epifanie, J. Sarrette, A. Gomes, and P. Teulet, "Simulation of radiative emission from nonequilibrium hypersonic nitrogen flows," in *29th AIAA, Plasmadynamics and Lasers Conference*, p. 2667, 1998.

[86] D. Baulch, D. Drysdale, and Horne, "Evaluated kinetic data for high temperature reactions," vol. 2, 1973.

[87] J. Parker, "Rotational and vibrational relaxation in diatomic gases," *The Physics of Fluids*, vol. 2, no. 4, pp. 449–462, 1959.

[88] S. M. Jo, O. J. Kwon, and J. Kim, "Master equation analysis and rotational relaxation time for N_2–N_2," in *AIAA Scitech 2020 Forum*, p. 1711, 2020.

[89] C. Park, "Assessment of a two-temperature kinetic model for dissociating and weakly ionizing nitrogen," *Journal of Thermophysics and Heat Transfer*, vol. 2, no. 1, pp. 8–16, 1988.

[90] D. Bose and G. V. Candler, "Simulation of hypersonic flows using a detailed nitric oxide formation model," *Physics of Fluids*, vol. 9, no. 4, pp. 1171–1181, 1997.

[91] D. Bose and G. V. Candler, "Advanced model of nitric oxide formation in hypersonic flows," *Journal of thermophysics and heat transfer*, vol. 12, no. 2, pp. 214–222, 1998.

[92] I. J. Wysong and S. F. Gimelshein, "Hypersonic non-equilibrium comparison cases," in *AIP Conference Proceedings*, vol. 2132, p. 100008, AIP Publishing LLC, 2019.

APPENDIX A

VERIFICATION OF THE QCT DIATOM-DIATOM SAMPLING STRATEGY AND Δv CUTOFFS

A.1 Convergence study of the allowable projectile vibrational states: N_2–N_2 system

The QCT sampling procedure, in which only the first few projectile vibrational states are resolved, is analyzed in this section. Specifically, a convergence study of the N_2–N_2 system is completed. For simplicity, an idealistic isothermal reservoir at 30,000K is used as the test case. This high temperature is chosen to exacerbate the influence of collisions with projectile molecules in high vibrational states. The isothermal reservoir is initialized in thermal and chemical nonequilibrium by setting a Boltzmann distribution of vibrational states at a 'cold' temperature of 300K and assuming only molecular nitrogen is present, thus 'mimicking' a post-shock state, in which the translational and rotational modes are quickly equilibrated at a high temperature, while the vibrational and chemical modes are assumed frozen through the shock front. The isothermal test case is simulated using the QCT rate coefficients obtained from allowing collisions with projectile molecules in vibrational quantum states 0, 0–1, 0–2, and 0–3 in order to assess the convergence of the transient thermo-chemical state of the gas. N_2–N collisions are neglected in this convergence study.

The vibrational temperature, T_v, and composition profiles are shown in Fig. A.1. The vibrational temperature is defined here as the temperature at which a Boltzmann distribution of vibrational states reproduces the instantaneous average vibrational energy of the system. It is apparent that the vibrational temperature profiles converge very quickly with the addition of more projectile vibrational states, and the influence of resolving additional projectile states is almost entirely negligible for dissociation, as all four composition curves nearly coincide. It is therefore concluded that limiting the initial projectile molecule to the first few vibrational states is an appropriate simplification for characterizing a full diatom-diatom system (at least for air species in the temperature

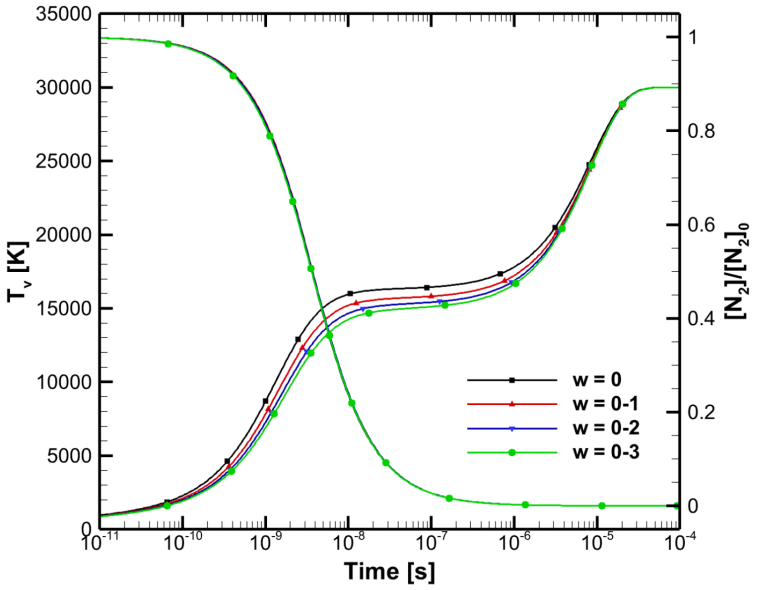

Figure A.1: Influence of resolving additional projectile molecule vibrational states, w, on vibrational excitation and dissociation in an isothermal reservoir of pure non-ionizing nitrogen, T = 30,000K. Dissociation profiles are nearly indistinguishable; hence, only one set of symbols is shown on their curves.

ranges of interest in this study).

A.2 Convergence study of the allowable Δv: N_2–N_2 system

In addition to assuming collisions occur with molecules in the first several low-lying vibrational states, multi-quantum VT transitions are limited in diatom-diatom collisions. For N_2, the cutoff is chosen as $\Delta v \equiv |v - v'| = 20$. To ensure this cutoff is appropriate, a convergence study is completed. Isothermal reservoir simulations with a translational-rotational temperature of 30,000K are used for verification purposes, due to the high probability of multi-quantum transitions. Fig. A.2 shows the N_2–N_2 vibrational relaxation times as a function of the maximum vibrational quantum jump allowed. To define the asymptotic limit, the relaxation time is also computed considering all VT transitions. The vibrational relaxation time for $\Delta v \leq 20$ is approximately 6% slower than the relaxation time for which all VT transitions are included. This is an acceptable uncertainty that is equal to or smaller than the uncertainty of modern diagnostic techniques [7] .

The number of allowed transitions not only affects the macroscopic parameter of vibrational

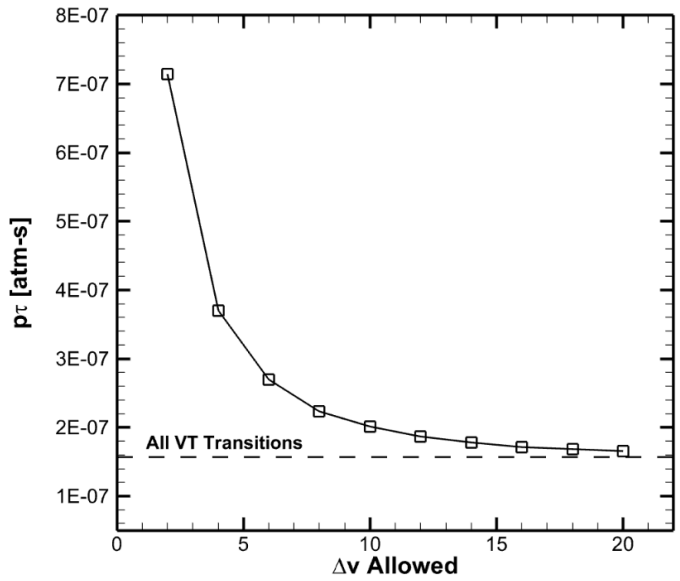

Figure A.2: Influence of resolving multi-quantum transitions on N_2–N_2 vibrational relaxation time, T = 30,000K.

excitation, but also the microscopic properties of the system — i.e. the vibrational state populations. As a direct result of this, the instantaneous rate of dissociation is altered. For this reason, an additional convergence study of vibrational state distributions and composition profiles is completed to ensure the Δv cutoff chosen is appropriate. Fig. A.3 shows the QSS vibrational state distributions in the isothermal reservoir simulations at T = 30,000K for a number of Δv cutoffs. As additional quantum jumps are considered, molecules are more readily pumped to the upper vibrational states to replenish those which are about to dissociate. $\Delta v \leq 20$ results in a nearly converged distribution when compared to the case for which all VT transitions are considered. Although not shown pictorially, the maximum instantaneous percent difference in mole fractions between the $\Delta v \leq 20$ case and the case considering all Δv transitions is less than 1%. Lower temperatures were also studied, where the differences noted are even smaller; therefore, it is concluded that $\Delta v \leq 20$ is an appropriate vibrational quantum jump cutoff for N_2–N_2 transitions in the temperature range of interest. Similar studies were also done to ensure the cutoff of $\Delta v \leq 10$ is appropriate for the O_2–O_2 collisional system in the temperature ranges of interest.

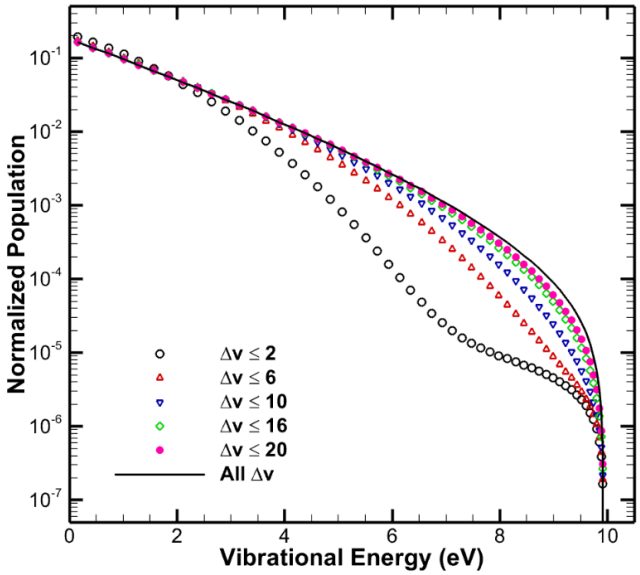

Figure A.3: Influence of resolving multi-quantum transitions on the quasi-steady state vibrational distribution, T = 30,000K. Only N_2–N_2 interactions are considered.